2022

Accretion Onto a Black Hole at the Center of a Neutron Star: Nuclear Equations of State

Sophia Christina Schnauck

Accretion Onto a Black Hole at the Center of a Neutron Star: Nuclear Equations of State

An Honors Paper for the Department of Physics and Astronomy

By Sophia Christina Schnauck

Bowdoin College, 2021

Abstract

A recent re-examination of Bondi accretion [47] revealed that, for stiff equations of state (EOSs), steady-state accretion can only occur for accretion rates exceeding a certain minimum. To date, this result has been explored only for gamma-law equations of state. Instead, we consider accretion onto a small black hole residing at the center of a neutron star governed by a more realistic nuclear EOS. We generalize the relativistic Bondi solution for such EOSs, approximated by piecewise polytropes, and thereby obtain analytical expressions for the accretion rates which were reflected in our numerical simulations. After taking several different piecewise EOSs at different neutron star densities into account, the accretion rates of the different EOSs were only slightly larger than the previously observed minimum. In other words there appears to be evidence for a nearly universal accretion rate that depends only on the black hole mass. However, we also observed that for certain densities the fluid profiles of several EOSs exhibited superluminal sound speeds outside the horizon of the black hole, suggesting that the EOSs are not appropriate at these densities.

Contents

Chapter 1

Introduction

1.1 Background

This thesis examines the accretion onto a small, non-rotating, possibly primordial black hole[1] inside of a neutron star. The motivation for this arises from previous work on the possibility of neutron stars effectively acting as dark matter detectors (see e.g. [14, 15, 16, 18, 23, 27, 28, 37]). For example, neutron stars may capture dark matter in the form of primordial black holes much less massive than the star, which may contribute to or comprise the dark matter in the Universe. These black holes could then accrete matter from the star until the star eventually collapses [31, 38]. Alternatively, the neutron star could also capture some other dark matter particles, possibly axions,[2] which under sufficiently favorable conditions may then collapse to form a black hole inside the star, resulting in the same scenario as above (see [15, 16, 37]). We refer to the black hole inside the neutron star as "endoparasitic", meaning that the black hole exhibits parasitic behavior by accreting the star from within it.

Some authors cite the observation of neutron star populations to constrain the abundance of primordial black holes to a mass range of about $10^{-15} M_\odot \lesssim M_{\rm BH} \lesssim 10^{-9} M_\odot$

[1] A primordial black hole is a black hole produced early in the Universe.

[2] The axion was postulated by Peccei–Quinn in 1977 as a hypothetical elementary particle which could resolve the CP-symmetry violation problem in quantum chromodynamics [22].

[18]. This mass window is poorly constrained by other arguments and observations (see e.g. [20, 19, 33, 49, 57]). For this constraint, both the capture rate of black holes and the accretion rate are important. The length of these rates determines whether we could even have observed such processes at the current age of the universe. The idea is that, if black holes did accrete neutron stars sufficiently quickly, we would not be able to observe any neutron stars today, even if there were many of them in the early universe. Thus the question of the survival time after which the entire star will be consumed by the black hole arises [8]. Answering it would help to constrain the contribution of s within the significant mass range to the dark-matter content of the Universe.

While other authors have determined different estimates of the rate of capture (see e.g. [18, 27, 40]), Schnauck, Baumgarte and Shapiro [50] (hereafter reffered toas SBS) establish rates for the accretion onto the black hole. The Bondi solution describes spherically symmetric steady-state accretion onto a static black hole. The Newtonian treatment by Bondi [13] is adequate for soft EOSs with adiabatic index $\Gamma < 5/3$. Stiff EOSs ($\Gamma > 5/3$), like those describing the interior of a neutron star, require a relativistic treatment for the accretion onto a Schwarzschild black hole[3] as shown by Richards, Baumgarte and Shapiro [47].[4]

East and Lehner, among others, performed numerical simulations of accretion onto endoparasitic black-holes residing in a neutron star [23]. They determined the accretion rates for three nuclear EOSs for large black hole masses on the order of magnitude of 10^{-2} neutron star masses. They determined that the effects of rotation of a black hole on the accretion rate are small.

The research for this thesis centers on determining how fast these processes may occur. We performed numerical simulations of the accretion process of the neutron star onto the "endoparasitic" black hole and generalized results of Richards, Baumgarte

[3]A Schwarzschild black hole is a static black hole, i.e. it does not rotate (has no angular momentum) and does not have electric charge.

[4]Previous works considered focused on soft EOSs with an adiabatic index $1 \leq \Gamma \leq 5/3$ [39, 51].

and Shapiro (2021a) and Richards, Baumgarte and Shapiro (2021b) [47, 48]. The main difference between our work and that of Richards, Baumgarte and Shapiro (2021a)lies in the use of realistic nuclear EOSs approximated by piecewise polytropes rather than a single Gamma-law equation of state.

1.2 Summary

A recent re-examination of Bondi accretion by Richards, Baumgarte and Shapiro (2021a) and (2021b), revealed that, for stiff equations of state (hereafter reffered toas EOSs), steady-state accretion is possible only for accretion rates larger than a certain minimum accretion rate. Since neutron stars are governed by stiff EOSs, this result is relevant for accretion onto black holes that might reside at the center of such stars. To date, this new result has been explored only for gamma-law EOSs. In this project we performed numerical simulations for a family of realistic nuclear EOSs and explored the emergence of a nearly universal minimum accretion rate. The numerical results obtained agreed very well with those determined analytically in [50].

In Chapter 2, we introduce polytropic EOSs as well as nuclear EOSs and their piecewise approximations as described by Read et al. (2009) [45]. We use and then add onto the assumption by Read et al. (2009) that EOSs can be described well by only one parameter, i.e. they are governed by cold temperatures, by considering a thermal correction to allow for heating. Instead we use two parameters to describe the pressure inside the neutron star in order to consider warm temperatures as well. For the research the thesis was based on we chose representatives of four different families of EOSs namely, SLy, AP3, AP4, MS1 and H4 (see [45]).

The numerical implementation of the code used, and tests of said code, are introduced in Chapter 3. All simulations are carried out in spherical polar coordinates, as in [3, 4]. The radial grid points are logarithmically implemented in order to accommodate

the large difference in the length scales between the neutron star and the tiny black hole residing in it. We use small black hole masses in order to reflect the expected mass range of primordial black holes. Additionally we discuss some unit conversions of entities such as the pressure and central density from the geometrized units used in the code to the more common cgs-units.

We describe our numerical results in Chapter 4. All simulations are made in the realm of general relativity and extend the work of East and Lehner [23] and of course Richards, Baumgarte and Shapiro (2021a) and (2021b). The work of Richards, Baumgarte and Shapiro (2021b) considered stiff single Gamma-law EOSs, which is extended in our research by implementing realistic EOSs approximated by piecewise polytropes. East and Lehner [23] used a similar approach for the EOSs but performed simulations for larger black hole masses only, outside of the range of PHBs or dark matter black hole candidates.

Chapter 5 explores the analytical solutions derived for stationary accretion rates onto small Schwarzschild black holes for the piecewise polytropic case. We find excellent agreement with the numerical results of Chapter 4. The analytical results described in this chapter are a generalization of those in Richards, Baumgarte and Shapiro (2021a), where they were not discussed for piecewise polytropes.

In Chapter 6 we summarize our findings, namely that for realistic nuclear EOSs the accretion rates depend mainly on the mass of the black hole and only slightly on the mass of the neutron star. The accretion rate determined in our approach is only slightly larger than the minimum value reported by [8] for Gamma-Law EOSs. We also discuss the occurrence of superluminal sound speeds outside the horizon of the black hole for certain lower densities for several of the EOSs.

1.3 Contributions

This thesis is based on the collaborative work which resulted in the publication of Schnauck, Baumgarte and Shapiro (2021), which I have previously abbreviated as SBS. My main contributions to this work, in this thesis are:

- The numerical implementations and tests in Chapter 3
- The numerical simulations and solutions in Chapter 4
- The data for the graphs in Chapter 3 as well as the sound speed graph in Chapter 6
- The Tables 3.3, 3.4 and most entries in Table 6.1

Chapter 2

Equation of State

2.1 Polytropic equations of state

In general EOSs relate the pressure and rest-mass density of a gas to one another[1]. Neutron stars may be modelled by so-called polytropic EOSs. A polytrope is accordingly a star governed by a polytropic EOS. The expression for this polytropic relation between a gas's density and pressure is given by

$$P = K\rho_0^{\Gamma}, \tag{2.1}$$

where the adiabatic index Γ describes the stiffness of the equation and K is the polytropic gas constant. A variety of stars can be modeled as polytropes. The pressure inside white dwarfs is dominated by non-relativistic degenerate electrons. In this case we consider $\Gamma = 5/3$. In the extreme limit these electrons would be relativistic, such that $\Gamma = 4/3$ [6, 51]. These examples can also be generalized for any fermion, such as the neutron.

Previous considerations of Newtonian Bondi accretion, or relativistic Bondi accretion onto a black hole dealt with soft EOSs. For the purpose of this thesis we will call EOSs with an adiabatic index $\Gamma < 5/3$ soft, as the Newtonian solution only holds

[1]The words gas and fluid can be used interchangeably here.

for such Γ. However, although we know little about the EOS governing the neutron star core, most realistic candidates for the EOS at nuclear densities have $\Gamma > 5/3$, which we will call stiff. Thus, all the EOSs discussed in this thesis will be stiff, i.e. an increase in the density ρ_0 leads to a large increase in the pressure P. Richards et al. [47] performed simulations of the accretion rates under the assumption of Γ-law EOSs, which are governed by the polytropic EOS for $\Gamma \geq 5/3$ and provided a specific example for the $\Gamma = 2$ case. However, a realistic neutron star do not satisfy this Γ-law EOS, which lead us to choose an approach with a nuclear EOSs instead.

2.2 Nuclear equations of state

A simple calculation shows that the density inside neutron stars is similar to that of nucleons. Assume for simplicity a neutron star is a perfect sphere of a radius of about $12\text{km} = 1.2 \times 10^6\text{cm}$. Thus it would have a volume of

$$V_{\text{NS}} = \frac{4\pi}{3} r^3 \approx 7.2 \times 10^{18}\text{cm}^3. \tag{2.2}$$

Thus, assuming the neutron star mass to be about $M_{\text{NS}} = 1.4 M_\odot \approx 3 \times 10^{33}\text{g}$, we can compute the rest-mass density inside the neutron star as follows:

$$\rho_{\text{NS}} = \frac{3 \times 10^{33}\text{g}}{7.2 \times 10^{18}\text{cm}^3} \approx 4 \times 10^{14}\text{g cm}^{-3}. \tag{2.3}$$

Now let us compare this value to the density inside the neutron itself, assuming a neutron's mass to be $m_{\text{neutron}} = 1.67 \times 10^{-24}\text{g}$ and its radius to be $r_{\text{neutron}} = 0.8 \times 10^{-13}\text{cm}$. This gives us a volume of

$$V_{\text{neutron}} = \frac{4\pi}{3} r_{\text{neutron}}^3 \approx 2 \times 10^{-39}\text{cm}^3 \tag{2.4}$$

and hence a density of

$$\rho_{\text{neutron}} = \frac{1.67 \times 10^{-24}\text{g}}{2 \times 10^{-39}\text{cm}^3} \approx 8 \times 10^{14}\text{g cm}^{-3}. \tag{2.5}$$

In other words ρ_{neutron} and ρ_{NS} are on the same order of magnitude. Thus the neutron star has densities in the range of nuclear matter meaning that a nuclear equation of state is required to model it. However, while we know that neutron stars can be represented by nuclear matter, determining the EOS which describes this realistically is challenging.

We know that in the observable universe, neutron stars display matter with the highest densities. This high density, poses exceptional challenges in trying to understand them, as we can not replicate such high densities here on Earth. Most realistic EOS candidates are stiff, although we do not know much about the EOSs at the core of neutron stars. Different approaches to model the behavior of the matter in the star at nuclear densities can be chosen, yielding a variety of realistic EOS for cold nuclear matter. This matter may be approximated with piecewise polytropes, as in Read et al. (2009) [45]. In SBS we generalize the results of Richards, Baumgarte and Shapiro (2021a) and (2021b) as well as [23] using nuclear EOSs, approximated by piecewise polytropes.

2.3 Piece-wise Polytropes as Approximation for Nuclear EOSs

Read et al. (2009) state that neutron-stars can by described accurately using cold nuclear EOSs with only one-parameter [45]. Generally we would describe the pressure of a system through two parameters, namely its density and temperature. In neutron stars we may however neglect the temperature if it is small compared to the Fermi temperature. We adapt the approach of Read et al.(2009) by using an EOS with one parameter and then considering a correction for thermal components, assuming that the latter is much smaller

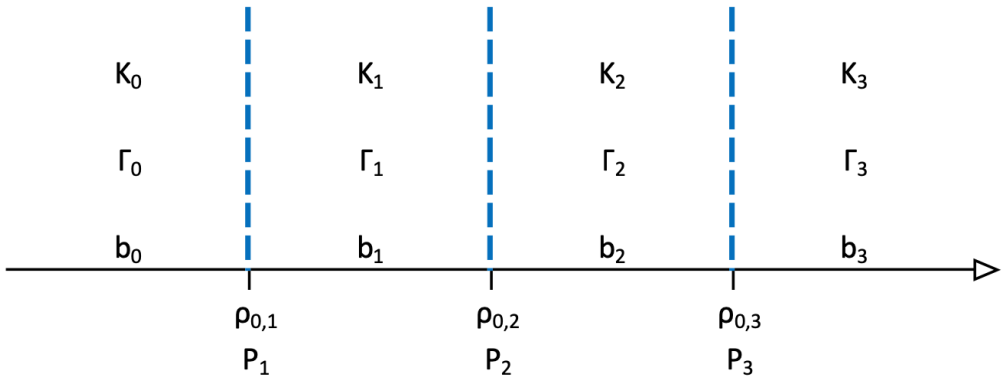

Figure 2.1: This diagram depicts the values of constants K_i, the adiabatic indices Γ_i and the integrations constants b_i (computed in equation 3.5) in four density regions. In a range from $0 \leqslant \rho_0 \leqslant \rho_{01}$ we use the values K_0 and b_0. Then from $\rho_{01} \leqslant \rho_0 \leqslant \rho_{02}$ we use the values K_1 and b_1, from $\rho_{02} \leqslant \rho_0 \leqslant \rho_{03}$ we use the values K_2 and b_2 and then finally for $\rho_0 \geqslant \rho_{03}$ we use K_3 and b_3.

than the former (see section 2.4).

A major challenge with such nuclear EOSs is that there is a substantial uncertainty. For the pressure for example, the uncertainty is potentially as large as an order of magnitude (see [45]). This is because little is known about the interior make-up of the neutron star, i.e., which phase of matter to expect. This allows for EOS candidates for a variety of different particles inside the star's core such as nucleons, hyperons, pions and kaons as well as strange quark matter (see Fig. 2.2).

The parametrized EOS is determined by the neutron stars' properties in each of four different density regions we label with indices $0 \leq i \leq 3$. These density regions are separated by three "boundary densities" (see Fig. 2.1). The stiffness, i.e. the adiabatic index Γ_i is determined in each region, where $\Gamma_i = d(\log P_i)/d(\log \rho_{0,i})$. Additionally, we fix the pressure at one boundary density, in our case P_2. Below the nuclear density the EOS is matched to some known low-density EOS. We then express the pressure of the

	ρ_0 [g cm^{-3}]	ρ_0 [$M_\odot^{-2}$]
$\rho_{0,1}$	1.46×10^{14}	2.37×10^{-4}
$\rho_{0,2}$	5.01×10^{14}	8.11×10^{-4}
$\rho_{0,3}$	1.00×10^{15}	1.62×10^{-3}

Table 2.1: The values of the boundaries rest-mass densities separating the four regions of Fig. 2.1 are given in cgs and geometrized units. For each i, the constants Γ_i, K_i, and b_i are appropriate between the densities $\rho_{0,i}$ and $\rho_{0,i+1}$. A note on the units of these densities is given in Chapter 3 (see also SBS).

neutron star as a function of the rest-mass density ρ_0 as follows:

$$P_i = K_i \rho_0^{\Gamma_i} \tag{2.6}$$

where K_i are different constants in each region. We show why this holds below.

The three adiabatic indices and one of the K_i for each respective EOS candidate can be found from fits. The remaining K_i can be determined by imposing continuity of the pressure P at each of the boundary densities starting with the fixed pressure described above (this will be explained in more detail in Chapter 3). The three boundary densities can be chosen to be the same for every EOS and take on the values given in Table 2.1.

The first law of thermodynamics is given by

$$dQ = d\left(\frac{\rho}{n}\right) + Pd\left(\frac{1}{n}\right) \tag{2.7}$$

(see, e.g., Shapiro and Teukolsky [51], hereafter ST) where dQ is the heat gained per baryon, $1/n$ is volume per baryon and ρ is the total mass-energy density. In our case we observe adiabatic processes, so we can assume that $dQ = 0$, which implies

$$d\left(\frac{\rho}{n}\right) = -Pd\left(\frac{1}{n}\right) \tag{2.8}$$

where we may replace n by ρ_0 as $\rho_0 = nm_b$,

$$d\left(\frac{\rho}{\rho_0}\right) = -Pd\left(\frac{1}{\rho_0}\right). \tag{2.9}$$

where we have $\rho_{0,i-1} \leq \rho_0 \leq \rho_{0,i}$. Then with equation (2.6) and the above we have

$$d\left(\frac{\rho}{\rho_0}\right) = -K_i\rho_0^{\Gamma_i}d\left(\frac{1}{\rho_0}\right). \tag{2.10}$$

By integrating (where $\Gamma_i \neq 1$) we obtain

$$\frac{\rho}{\rho_0} = (1 + b_i) + \frac{1}{\Gamma_i - 1}K_i\rho_0^{\Gamma_i - 1} \tag{2.11}$$

which then implies

$$\rho = \rho_0 + b_i\rho_0 + \frac{K_i}{\Gamma_i - 1}\rho_0^{\Gamma_i} \tag{2.12}$$

where b_i are the constants of integration. In general we have $b_i \neq 0$, but in the least density region we have $\lim_{\rho_0 \to 0} \frac{\rho}{\rho_0} = 1$ and thus $b_0 = 0$. We now choose the b_i so that energy density ρ is continuous across the boundaries. Specifically, we evaluate ρ at the boundary between regions $i - 1$ and i twice, once using values in region $i - 1$ (yielding the value $\rho(\rho_{0,i})$) and once in region i using the expression (2.12). This results in

$$b_i = \frac{\rho(\rho_{0,i})}{\rho_{0,i}} - 1 - \frac{K_i}{\Gamma_i - 1}\rho_{0,i}^{\Gamma_i - 1}. \tag{2.13}$$

Read et al.(2009) call the integration constants a_i; however, we wish to avoid confusion with the sound speed discussed later. From this we can now compute the specific internal energy ϵ, where we have the relation $\epsilon = \rho/\rho_0 - 1$:

$$\epsilon = b_i + \frac{K_i}{\Gamma_i - 1}\rho_0^{\Gamma_{i-1}} \tag{2.14}$$

(see eq. 6 in Read et al. (2009). Now we may compute the sound speed a under the assumption of constant entropy as follows:

$$a^2 = \left(\frac{dP}{d\rho}\right)_s = \frac{\rho_0}{\rho + P}\left(\frac{dP}{d\rho_0}\right)_s = \frac{\rho_0}{\rho + K_i\rho_0^{\Gamma_i}}\left(\frac{d(K_i\rho_0^{\Gamma_i})}{d\rho_0}\right)_s$$

$$= \frac{\rho_0}{\rho_0 + b_i\rho_0 + K_i\rho_0^{\Gamma_i}/(\Gamma_i - 1) + K_i\rho_0^{\Gamma_i}} \times (\Gamma_i K_i \rho_0^{\Gamma_i - 1})$$

$$= \frac{\Gamma_i K_i \rho_0^{\Gamma_i - 1}}{1 + b_i + K_i\rho_0^{\Gamma_i - 1}(\Gamma_i - 1) + K_i\rho_0^{\Gamma_i - 1}}$$

$$= \frac{\Gamma_i K_i \rho_0^{\Gamma_i - 1}}{1 + b_i + \Gamma_i K_i\rho_0^{\Gamma_i - 1}/(\Gamma_i - 1)}. \tag{2.15}$$

We can then invert this and obtain the following

$$\Gamma_i K_i \rho_0^{\Gamma_i - 1} = \frac{a^2(1 + b_i)}{1 - a^2/(\Gamma_i - 1)}. \tag{2.16}$$

While the pressure P, internal energy density ϵ and total mass-energy density ρ are continuous across each of the four regions, the sound speed a will not necessarily be, as we will see later in Chapter 5 or graphically in Chapter 6.

Read et al. (2009) list a series of EOS candidates that we may approximate with the parametrized EOS as described above. We considered representatives of four families of EOSs. Each of these EOS families represent a different way (or a different physical theory) of creating a candidate for a realistic nuclear EOS. First, the SLy, AP3, AP4 and MS1 EOSs are for nuclear matter, i.e. neutrons, protons, electrons and muons ($npe\mu$). The SLy EOS is an example of the so-called potential-method family [21]. Both AP3 and AP4 are so-called variational-method EOSs [1]. MS1 is a relativistic mean field theory EOS MS1 [42]. These four EOSs, made up of ($npe\mu$) matter in Fig. 2.2, are represented

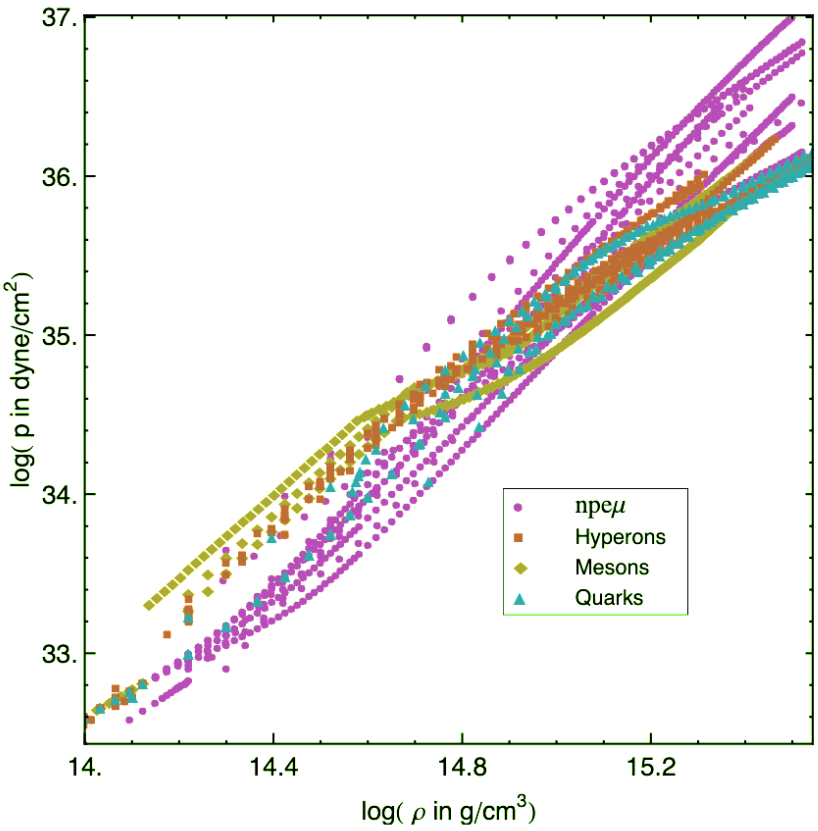

Figure 2.2: Figure 1 in Read et al. (2009) [45] shows pressure versus rest-mass density for various candidate EOSs. Note that Read et al. use ρ for the rest-mass density, while we use ρ_0. The different EOSs are grouped as indicated in the label.

by the pink circles.

The H4 EOS belongs to the group of EOS models with hyperons, pion and kaon condensates and quark matter at their cores. Specifically it is an relativistic mean field theory EOSs with hyperons[35]. In Fig. 2.2 it is represented by orange squares.

Most generally these different EOSs lead to a wide range of pressures for a given rest mass density which will be considered in the piecewise polytrope approach (see Fig. 2.2).

2.4 Thermal and Cold Contributions

The EOSs discussed so far are "cold", meaning that they assume zero temperature. Although our initial data begin by describing a cold gas, we allow for heating (e.g. by shocks) by introducing additional thermal contributions to the cold pressure. Specifically, we compute thermal contributions to the internal energy density $U \equiv \rho_0 \epsilon$, where $\epsilon = \epsilon_{\rm th} + \epsilon_{\rm cold}$, as the sum of a thermal and a cold component as follows:

$$U = U_{\rm th} + U_{\rm cold}$$

Thus we have

$$U_{\rm th} = U - U_{\rm cold} = \rho_0(\epsilon - \epsilon_{\rm cold}), \tag{2.17}$$

where ρ_0 and ϵ are determined from the dynamically evolved quantities in our code, and $\epsilon_{\rm cold}$ is given by equation (2.14). In other words, the cold parts are approximated by the piece-wise polytropes, while the thermal parts in turn contain contributions both from the nucleons and the radiation. Thus we may then say $U_{\rm th} = U_{\rm nucl} + U_{\rm rad}$, where $U_{\rm nucl}$

accounts for finite-temperature corrections to an ideal, nonrelativistic, nucleon Fermi gas,

$$U_{\rm nucl} = \frac{(3\pi^2)^{1/3} m_{\rm B}}{6\hbar^2} n^{1/3} (k_{\rm B}T)^2, \tag{2.18}$$

and $U_{\rm rad}$ for contributions from radiation,

$$U_{\rm rad} = \eta a_{\rm rad} T^4 \tag{2.19}$$

(see [9]), where $m_{\rm B}$ is the baryon mass (we later use a value of 1.67×10^{-24}g), $n = \rho_0/m_{\rm B}$ is the baryon number density, $k_{\rm B}$ the Boltzmann constant, $\hbar$ Planck's constant, T the temperature, and $a_{\rm rad}$ the radiation constant. Additionally, the dimensionless constant η depends on which particles contribute to the radiation, where we allow for photons ($\eta_{\rm ph} = 1$), three flavors of neutrinos ($\eta_\nu = 3 \times 7/8$), as well as electron-positron pairs ($\eta_{\rm pairs} = 7/4$). Thus adding these particle's respective contributions we have $\eta = \eta_{\rm ph} + \eta_\nu + \eta_{\rm pairs} = 1 + 3 \times 7/8 + 7/4 = 43/8$ (see SBS).

Now, using all of the above we can determine the pressure P, made up of its thermal and its cold contributions, $P = P_{\rm cold} + P_{\rm th}$ and again the fact that the thermal contribution is made up of nuclear and radiative components. We then first obtain

$$P_{\rm th} = P_{\rm nucl} + P_{\rm rad} = (\Gamma_{\rm th} - 1)\, U_{\rm nucl} + \frac{1}{3} U_{\rm rad} \tag{2.20}$$

where $\Gamma_{\rm th} = 5/3$ for nonrelativistic nucleons. Thus we have

$$P = P_{\rm cold} + P_{\rm th} = P_{\rm cold} + (\Gamma_{\rm th} - 1)\, U_{\rm nucl} + \frac{1}{3} U_{\rm rad} \tag{2.21}$$

for the total pressure.

Chapter 3

Numerical Implementation and Tests

In this chapter I cross-check the validity of the numerical results by comparing certain parts of these results to already available data. For example, the maximal masses of the neutron stars could be compared with those found in Read et al. (2009). Other tests constituted graphs of the pressure by comparison to previous works, as well as viewing the sound speed (which we will only briefly discuss here, as it will be more relevant in Chapter 6).

3.1 Implementation

In order to implement the piecewise polytropic approach into the previously existing code structure, a derived class was implemented. The values of the constants used in the numerical calculations are given in Table **??** Now, for the purpose of converting units later, we also defined the mass of the sun in centimeters as the following:

$$M_{\odot}^{\mathrm{cm}} = \frac{G \cdot M_{\odot}^{\mathrm{g}}}{c^2} \approx 147662\,\mathrm{cm}.$$

Constant	Value
G	$6.67408 \times 10^{-8}\,\mathrm{cm^3\,g^{-1}\,s^{-2}}$
h	$6.62607 \times 10^{-27}\mathrm{cm^2\,g\,s^{-1}}$
c	$2.99792 \times 10^{10}\mathrm{cm\,s^{-1}}$
$M_\odot^{\mathrm{g}}$	$1.98847 \times 10^{33}\mathrm{g}$

Table 3.1: The table lists the constants used in the numerical calculations, where G is the gravitational constant, h is Planck's constant, c is the speed of light and $M_\odot^{\mathrm{g}}$ is the solar mass. Note that $\mathrm{cm^3\,g^{-1}\,s^{-2}}$ is the same as units of $\mathrm{dyn\,cm^2\,g^{-2}}$ and similarly $\mathrm{cm^2\,g\,s^{-1}}$ is the same as units of $\mathrm{erg\,s}$.

We will discuss the unit conversion further in Section 3.3 of this chapter.

Next let us recall that we have four density regions. For each EOS we are given, for example by Read et al. (2009), values for the four adiabatic indices Γ_i with $0 \leq i \leq 3$ which describe a respective type of parametrized EOS. Additionally we can obtain from Read et al. (2009) Table III, a value for $\log(P_2)$, from which we can obtain the pressure between the second and third density regions by imposing continuity.[1] Each EOS is thus characterized in our code by three values for Γ and by the respective P_2 (see Table 3.2). Note that Γ_0 is the same for each EOS and takes a value of $\Gamma_0 = 1.35692$.

From these values we can obtain the remaining information required to characterize our EOSs, starting with the constants K_i. As we know beforehand the value of the pressure at the boundary of regions $i = 1$ and $i = 2$ we can determine K_2 by invoking equation (2.6),

$$K_2 = P_2/\rho_{0,2}^{\Gamma_2}. \tag{3.1}$$

Recall that $\rho_{0,2}$ is the boundary rest-mass density. Having obtained a value for K_2 we can now determine the remaining K_i by imposing continuity of pressure and density between regions. For example at the boundary $i = 2$ we may evaluate the pressure P using the

[1] In Read et al. (2009) this value is in fact called $\log(p_1)$, however it corresponds to $\log(P_2)$ in our case.

EOS	Γ_1	Γ_2	Γ_3	K_0	K_1	K_2	K_3	b_1	b_2	b_3	$\log(P_2)$	P_2 [g cm^{-1} s^{-2}]
SLy	3.005	2.988	2.851	0.089492	84572.6	74935.5	31071.4	0.0104711	0.0102419	0.00234129	34.384	2.42×10^{34}
AP3	3.166	3.573	3.281	0.0747568	270916	4906280	751390	0.00888779	0.0128859	–0.00322345	34.392	2.47×10^{34}
AP4	2.83	3.445	3.348	0.0851938	18679.1	1486420	796972	0.00976174	0.0154307	0.011658	34.269	1.86×10^{34}
MS1	3.224	3.033	1.325	0.2032526	1970000	307447	5.26309	0.0243216	0.0175589	–1.66799	34.858	7.21×10^{34}
H4	2.909	2.246	2.144	0.194153	82323.1	735.161	381.707	0.0224696	-0.00640722	-0.0239386	34.669	4.67×10^{34}

Table 3.2: List of EOSs considered with their PWP parameters. The adiabatic coefficients Γ_i as well as the constants b_i are dimensionless, while, in geometrized units, the coefficients K_i have units of length (or mass) to the power $2(\Gamma_i - 1)$, which we express in units of solar mass. We use $\Gamma_0 = 1.35692$ in the lowest density region for all EOSs, adopting the value for the highest-density crust piece in [45] (see their Table II). Each EOS is determined through three different Γ_i for $1 \leq i \leq 3$. Additionally we must know one pressure, in our case P_2, in order to determine constants K_i and the remaining boundary pressures.

constants in either region $i = 1$ or $i = 2$. This results in the relation

$$K_1 = K_2 \rho_{0,2}^{\Gamma_2 - \Gamma_1}. \tag{3.2}$$

We similarly obtain

$$K_3 = K_2 \rho_{0,3}^{\Gamma_2 - \Gamma_3}$$
$$K_0 = K_2 \rho_{0,1}^{\Gamma_1 - \Gamma_0}.$$

Finally, having computed all the constants K_i, we can find the remaining boundary pressures:

$$P_1 = K_1 \rho_{0,1}^{\Gamma_1} \tag{3.3}$$
$$P_3 = K_3 \rho_{0,3}^{\Gamma_3}. \tag{3.4}$$

Now we must also determine the integration constants in equation (2.13). We know that $b_0 = 0$ (as discussed below equation (2.13)) for all EOSs. The remaining b_i however must be determined for each EOS individually. From continuity of ϵ we obtain

$$\begin{aligned} b_1 &= \frac{K_0 \rho_{0,1}^{\Gamma_0 - 1}}{\Gamma_0 - 1} - \frac{K_1 \rho_{0,1}^{\Gamma_1 - 1}}{\Gamma_1 - 1} \\ b_2 &= \frac{K_1 \rho_{0,2}^{\Gamma_1 - 1}}{\Gamma_1 - 1} - \frac{K_2 \rho_{0,2}^{\Gamma_2 - 1}}{\Gamma_2 - 1} + b_1 \\ b_3 &= \frac{K_2 \rho_{0,3}^{\Gamma_2 - 1}}{\Gamma_2 - 1} - \frac{K_3 \rho_{0,3}^{\Gamma_3 - 1}}{\Gamma_3 - 1} + b_2 \end{aligned} \tag{3.5}$$

using equation (2.13). After having determined the above and converted from cgs to geometrized units,[2] a series of routines are implemented to find among other observables, the pressure P for cold temperatures, the thermal pressure $P_{\rm th}$, the rest-mass density ρ_0

[2] A large part of the code is also dedicated to the conversion of all of the variables and quantities discussed above. A more thorough note on unit conversion is given in section 3.3.

and the sound speed a in the respective density regions.

3.2 Maximum Masses and other Tests

In order to better understand the behavior of our numerical results we compared them to those found by [21, 35], and Read et al [45]. We plot the rest masses as well as the total gravitational "ADM[3]" masses, which, in addition to the rest mass also include contributions from other forms of energies, and rest masses for the five EOSs, their sound speeds, pressures and internal energy densities in each of the density regions. We observed very good agreement of our data with that of for example Read et al [45].

3.2.1 Maximum Masses

We plot the maximal masses for the individual EOSs using the initial data for different values of the central density ρ_0. Generally our numerical data compared very well to the masses given in Table III of Read et al [45]. The maximum mass here refers to the maximal gravitational mass $M_{\max}^{\mathrm{ADM}}$ of the non-rotating neutron star. In Fig. 3.1 we observe a maximum at approximately $M_{\max}^{\mathrm{ADM}} = 2.06 M_{\odot}$. The value determined in Read et al. (2009) is slightly lower at $M_{\max,\,\mathrm{ref}}^{\mathrm{ADM}} = 2.049 M_{\odot}$.

The maximum masses for AP3, AP4 and MS1 EOS similarly agree well with the results of Read et al. (2009) (see Table 3.3).

3.2.2 Pressures

Both [21] and [35] list the pressure in correspondence to a baryon number density measured in fm^{-3}, whereas we would like to compare their results to the pressure as a function of the rest-mass density ρ_0. Thus we must first convert the baryon number

[3]ADM refers to Arnowitt, Deser and Misner (1962). We use it to denote the gravitational Arnowitt-Deser-Misner (ADM) mass. It is sometimes also referred to as mass-energy [6]

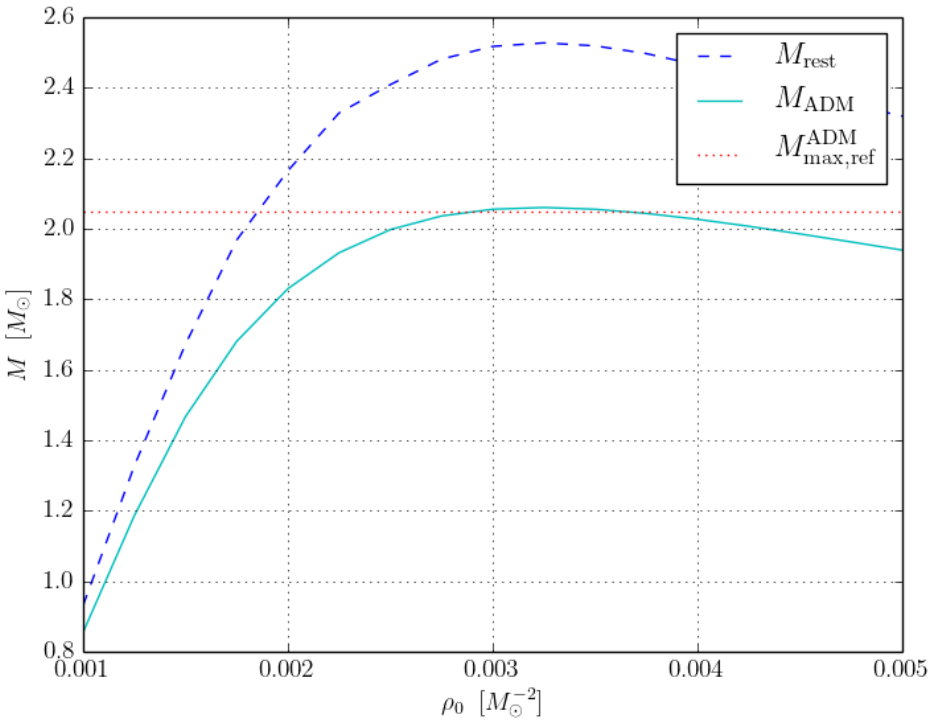

Figure 3.1: The graph shows $M_{\rm ADM}$ and $M_{\rm rest}$ for SLy EOS plotted as functions of the central rest-mass density ρ_0. We include for comparison the reference value $M^{\rm ADM}_{\rm max,ref}$, i.e. the maximal value of the mass according to Read et al.. The maximum ADM mass is obtained at $\rho_0 \approx 0.00325 M_\odot^{-2}$ and $M^{\rm ADM}_{\rm max} \approx 2.06 M_\odot$ in our simulations.

EOS	$M_{\max}^{\mathrm{ADM}}\,[M_\odot]$	$\rho_{0c}^{\max}[M_\odot^{-2}]$	$M_{\max,\,\mathrm{ref}}^{\mathrm{ADM}}\,[M_\odot]$
SLy	2.06	0.00325	2.049
AP3	2.38	0.00270	2.390
AP4	2.20	0.0031	2.213
MS1	2.74	0.00175	2.767
H4	2.00	0.003	2.032

Table 3.3: The maximum gravitational mass $M_{\max}^{\mathrm{ADM}}$ of non-rotating neutron stars, and the corresponding central density $\rho_{0c}^{\max}$ for each EOS are considered. We compare the maximum masses with those determined by Read et al. (2009) [45].

density n_b into the rest mass density. We assumed the baryon mass to be approximately $m_b = 1.7 \times 10^{-24}$g (although we are aware that this value is grossly rounded, it is sufficiently accurate to get a comparison between our data and the references')[4]. The conversion to ρ_0 is then quite straight forward:

$$\rho_0^{\mathrm{cgs}} = m_b n_b \times (10^{-13})^{-3}$$

where the factor $(10^{-13})^{-3}$ comes from the baryon number density being measured in fermi. We then convert this value into geometrized units. This conversion will be explained further in Section 3.3.

In Fig. 3.2 we see that the piece wise polytropic treatment agrees well with the tabulated data from [21]in each of the four regions.

3.3 Unit Conversion

In Read et al. (2009), all quantities are given in cgs units. Our code however use geometrized units instead, such that $G = c = 1$. This means all that the mass, length, and time quantities can each be expressed in terms of mass. We then finally fix the unit of mass by setting $M_\odot = 1$. Thus knowing the conversion between the unit systems is

[4]One might conclude that the previously mentioned issues with the mass of H4 EOS (and actually all of the H1-H4 EOSs) arises from this estimate, which is somewhat accurate for neutrons, but less so for hyperons which have a mass of about $m_{\mathrm{hyperon}} = 2.22 \times 10^{-24}$g, this does not however resolve the problem.

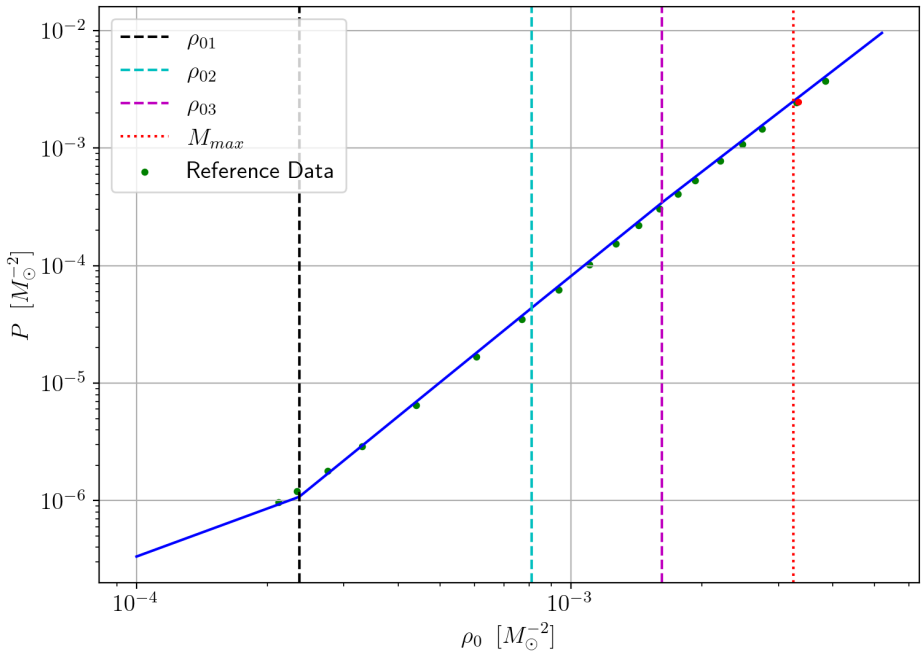

Figure 3.2: The SLy EOS pressure in $[M_\odot^{-2}]$ is plotted as a function of rest-mass density and compared with reference data from [21]. The pressure for the maximum mass of the neutron star is of order of magnitude 10^{-3}. As the values Γ_2 and Γ_3 for SLy EOS are very similar we cannot easily observe the piecewise nature of the above graph.

necessary. We will denote the quantities with a superscript of cgs, e.g. ρ_0^{cgs}, the code units will be marked with a bar, e.g. $\bar{\rho}_0$.

Using the values for the physical constants given in table 3.1

$$\frac{GM_\odot}{c^2} = 1.47663 \times 10^5 \text{cm}. \tag{3.6}$$

Thus we have $M_\odot = 1.47663 \times 10^5$cm in geometrized units, as we know $G = c = 1$.

We now convert the units of the density, ρ_0, the pressure P, the energy density ρ and the constant K. First ρ_0^{cgs} has units of g/cm^3 i.e.

$$[\rho_0^{\text{cgs}}] = \frac{\text{g}}{\text{cm}^3},$$

	ρ_0	P	K
cgs	2.01×10^{15}	1.907×10^{35}	3.276×10^{-8}
geometrized	3.25×10^{-2}	3.436×10^{-3}	31071.4

Table 3.4: The values of the rest-mass density ρ_0, ρ, pressure P, and K are given in both cgs and geometrized units. The example calculations are for SLy EOS in the maximum mass region (see Fig. 3.1)

Thus it follows that

$$\left[\frac{G\rho_0^{\text{cgs}}}{c^2}\right] = \text{cm}^{-2},$$

This means that in geometrized units, we may express the density in units of $M_\odot^{-2}$,

$$\bar{\rho}_0 = \frac{G}{c^2}\left(\frac{1.47663 \times 10^5 \text{cm}}{M_\odot}\right)^2 \rho_0^{\text{cgs}}. \tag{3.7}$$

The pressure P has units of dynes $\text{cm}^{-2} = \text{g}\,\text{cm}^{-1}\,\text{s}^{-2}$. If we multiply it by G/c^4 we can express it in units of $M_\odot^{-2}$ again:

$$\bar{P} = \frac{G}{c^4}\left(\frac{1.47663 \times 10^5 \text{cm}}{M_\odot}\right)^2 P^{\text{cgs}}. \tag{3.8}$$

The energy density ρ has the same units as the pressure P which we found the conversion for above. Hence it can be expressed in geometrized units the same way, i.e

$$\bar{\rho} = \frac{G}{c^4}\left(\frac{1.47663 \times 10^5 \text{cm}}{M_\odot}\right)^2 \rho^{\text{cgs}}. \tag{3.9}$$

In order to determine K in code units we first note that

$$[K^{\text{cgs}}] = \frac{\text{g}^{1-\Gamma}\,\text{cm}^{3\Gamma-1}}{\text{s}^2} \tag{3.10}$$

where Γ is the adiabatic index. The reason for the above units for K is that in order to receive the correct units of g cm^{-1} s^{-2} for the pressure P, and given units of g cm^{-3} for the rest-mass density ρ_0 we must satisfy equation (2.6). Thus Γ will influence the units

of K. Using the above expression (3.10), we can say

$$\left[G^{1-\Gamma}c^{2\Gamma-4}K^{\text{cgs}}\right] = \text{cm}^{2\Gamma-2}.$$

In order to find $\bar{K}$ in geometrized units we compute

$$\bar{K} = G^{1-\Gamma}c^{2\Gamma-4}\left(\frac{M_\odot}{1.47663\times10^5\,\text{cm}}\right)^{2\Gamma-2}K^{\text{cgs}}. \tag{3.11}$$

Now let us calculate an example conversion, with quantities from SLy EOS, where $P_2^{\text{cgs}} = 10^{34.384}\,\text{g}\,\text{cm}^{-1}\,\text{s}^{-2} = 2.42103\times10^{34}\,\text{g}\,\text{cm}^{-1}\,\text{s}^{-2}$ and $\rho_{02}^{\text{cgs}} = 5.01187\times10^{14}\,\text{g}\,\text{cm}^{-3}$ at the border between regions 1 and 2 (note that this is called P_1 in Read et al. (2009)) and $\Gamma_1 = 3.005$.[5] Then from these values we find K_1 as follows:

$$K_1^{\text{cgs}} = \frac{P_2}{\rho_{02}^{\Gamma_1}} = 1.624\times10^{-10}\,\text{cgs}.$$

Using the conversion for K we found above we have

$$\bar{K}_1 = 8.6222\times10^4 M_\odot^{2\Gamma-2}.$$

Thus using $\bar{K}_1$, $\bar{\rho}_{02} = 8.03\times10^{-4}\,M_\odot^{-2}$ and the values of the variables for SLy EOS, we have

$$\bar{P}_2 = \bar{K}_1\bar{\rho}_{02}^{\Gamma_1} = 4.319\times10^{-5}M_\odot^{-2}.$$

Then we can convert this back to cgs units and obtain the expected result using (3.8):

$$P_2^{\text{cgs}} = 2.42\times10^{34}\text{dynes}\,\text{cm}^{-2}$$

At this point we know the conversion of most of our relevant quantities from cgs to code units. Note that the specific internal energy density ϵ and the constants b_i are

[5] see Fig. 2.1

dimensionless, so $\bar{\epsilon} = \epsilon^{\rm cgs}$ and $\bar{b}_i = b_i^{\rm cgs}$.

Chapter 4

Numerical Simulations

To determine the accretion rate onto the endoparasitic black hole at the center of the neutron star we performed numerical simulations. Previously, East and Lehner (2019) considered the accretion onto black holes of masses $M_{\rm BH} \geq 10^{-2} M_{\rm NS}$ embedded in the neutron star, for nuclear EOSs with the piecewise polytrope approach and found that the accretion rate is proportional to the square of the black hole mass [23]. They also determined that rotational effects are small. In Richards, Baumgarte and Shapiro (2021b) simulations for non-rotating black holes with smaller black hole masses ($M_{\rm BH} \gtrsim 10^{-9} M_{\rm NS}$) for stiff Γ-law EOSs were performed. We now extend the work of [23], Richards, Baumgarte and Shapiro (2021a) and (2021b) . The numerical code used to obtain the data for this thesis as well as [50] is described further in [3] and [4]. In general the simulations consist of two steps, namely the construction of initial data and then the numerical evolution of these data.

4.1 Initial Data

The initial data for this thesis and SBS are similar to those of RBSa and RBSb, in all ways but one: instead of the Gamma-law approach we use nuclear EOSs. The initial data are constructed using solutions to the Tolman-Oppenheimer-Volkoff equations for a

specific central density [44, 55], which describe a non-rotating equilibrium neutron star. As in Richards, Baumgarte and Shapiro (2021b) , the generalized puncture method is used to place a black hole of puncture mass[1] $\mathcal{M}$ at the center of the neutron star. Then, assuming a moment of time symmetry, the Hamiltonian constraint for the conformal factor ψ is solved in order to obtain solutions of Einstein's constraint equations (see e.g [6, 7]). We assume the initial data to be conformally flat, i.e. $\gamma_{ij} = \phi^4 \eta_{ij}$, where η_{ij} is a flat metric[2]. As we assumed a moment of time symmetry, we know the momentum constraint is satisfied identically, as all time derivatives are zero, and we are left with the Hamiltonian constraint (the non-linear Poisson equation), namely

$$\bar{D}^2 \psi = -2\pi \psi^5 \rho_{\mathrm{ADM}}, \tag{4.1}$$

where D^2 is the flat Laplace operator, ∇^2. For $t = 0$ the ADM-density $\rho_{\mathrm{ADM}} = \rho$, the total energy density. Now ρ can be expressed as $\rho = \psi^m \bar{\rho}$, so equation (4.1) becomes the following:

$$\nabla^2 \psi = -2\pi \psi^{5+m} \bar{\rho}. \tag{4.2}$$

Note that a definite answer is guaranteed only if the sign of exponent of ψ is negative, i.e. the factor and the exponent share a sign. This occurs for $m < -5$.

As shown in section III.C.1 of Richards, Baumgarte and Shapiro (2021b) the black hole's gravitational mass is well approximated by $M_{\mathrm{BH}} \simeq \psi_{\mathrm{NS}} \mathcal{M}$ for $\mathcal{M} \ll M_{\mathrm{NS}}$, where ψ_{NS} is the conformal factor at the center of the unperturbed neutron star.

The initial data used to evolve our data are similar to those in Richards, Baumgarte and Shapiro (2021a) and (2021b) , however we make use of the piecewise polytrope approach as explained in Chapter 3. The initial data describe a cold gas, however, as

[1] $\mathcal{M}$ acts as a parameter for the mass without any a priori physical meaning.

[2] Here flat means that the Riemann curvature tensor vanishes. See [7] for a textbook explanation.

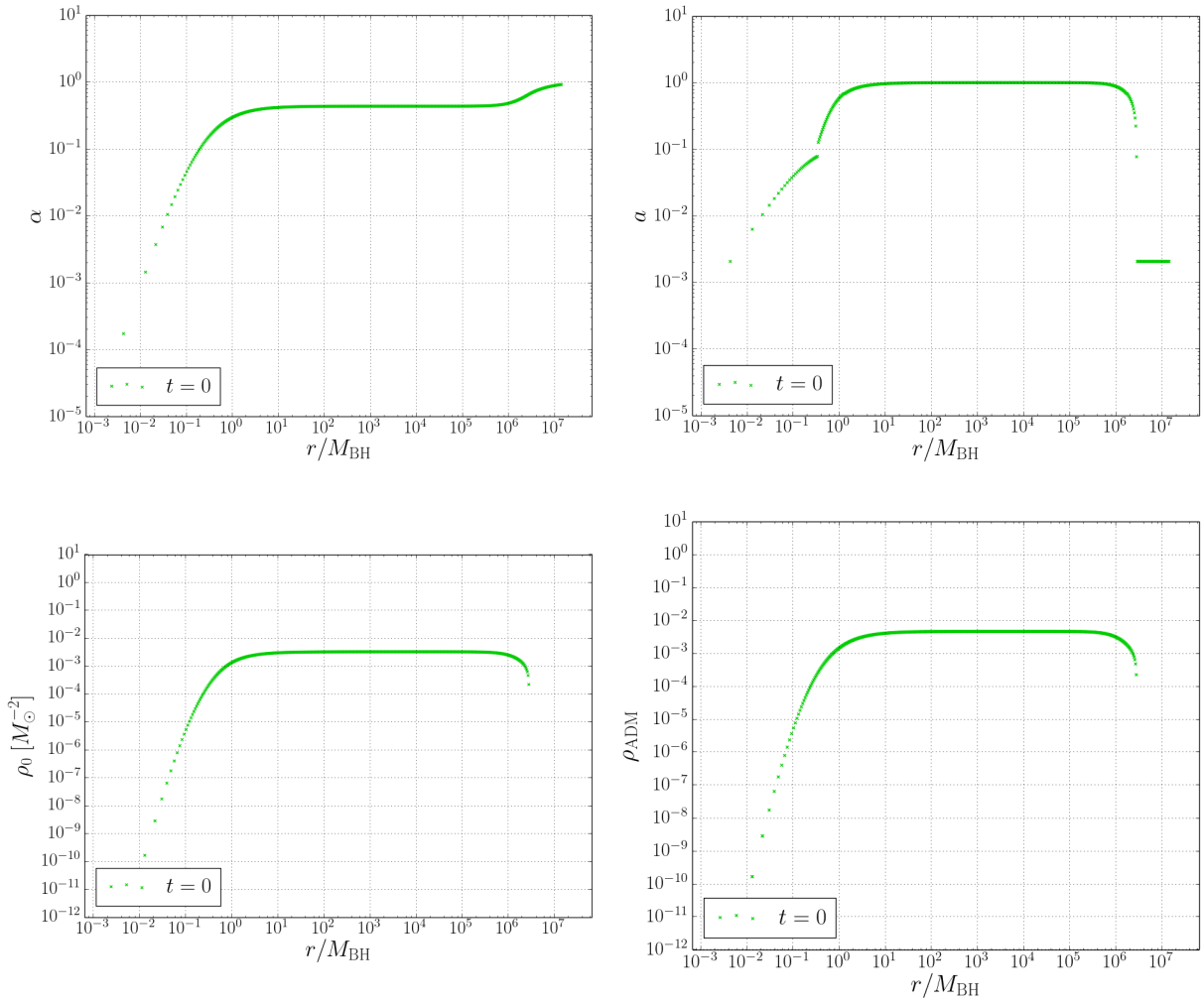

Figure 4.1: Profiles of several quantities describing the initial data for a black hole embedded in a neutron star of central rest-mass density $\rho_0 = 0.00325 M_\odot^{-2}$, governed by the SLy EOS. I show the lapse α in the top left panel, the sound speed a in the top right, rest-mass density ρ_0 in the bottom left and the total energy density $\rho_{\rm ADM}$ in the bottom right, all shown as a function of the radius r. Note the kink in the plot of the sound speeed a is a result of the discontinuity or jumps in the values for Γ_i.

explained in Chapter 3 we later account for heating (for example through shocks) in the numerical evolution.

In Fig. 4.1 we show the initial data for SLy EOS at a central density of 1.99×10^{15}g cm^{-3}. The lapse α, which measures the ratio between the advance of proper time and coordinate time, is shown in the top left of Fig. 4.1. Note that the initial sound speed a in the top right panel of 4.1 never quite reaches the speed of light (recall $c = 1$ here).

Our initial data are astrophysically artificial since they do not represent equilibrium solutions. Thus we must evolve the initial data to obtain an equilibrium solution and the relevant data.

4.2 Numerical Evolution Data

The numerical evolution was carried out using the Baumgarte-Shapiro-Shibata-Nakamura (BSSN) formalism of the Einstein equations ([5, 6, 43, 52]) in spherical polar coordinates [4, 12]. This is done with the help of a reference-metric formalism [12, 17, 29, 53]. The lapse and the shift, made up of three spatial components, determine the coordinates of the four dimensional space-time. A "Gamma-driver" condition for the shift and a "1+log" slicing for the lapse [2, 11, 54] are implemented to specify the lapse and the shift. We start with a "pre-collapsed" lapse $\alpha = \psi^{-2}$ and a vanishing shift as initial data for these coordinate conditions. The code makes use of a fourth-order Runge-Kutta method to integrate over the time as well as fourth-order finite differencing to determine the spatial derivatives of the Einstein equations.

Using a Harten-Lax-van-Leer-Einfeldt approximate Riemann solver (see [30] and [24]) along with a simple monotonized central-difference limiter reconstruction scheme [56] we evolve the relativistic hydrodynamical equations.

The numerical sound speeds that are used in the approximate Riemann solver[3] and

[3]The Riemann solver is a numerical method used to solve a Riemann problem, i.e. an initial value

the process of transforming the sound speed from one reference frame (the fluid frame) to another (the coordinate frame) may result in taking the square root of a negative value. This would make our code crash. To avoid this several different approaches were considered, such as artificially assuming this negative root to be zero. All of the approaches exhibited little difference from one another (see SBS).

In all simulations we observe a transition from the initial data to the equilibrium solution for the accretion onto the black hole inside the star. In the case of smaller central densities used to form the initial data this transition creates a shock wave, which can be followed through the time evolution (see e.g. Fig.4.2). The accretion solution is then realized inside this shock. Although some heating may occur due to the shock wave, we have found it to be small especially for larger initial densities. Additionally this heating seems to be short-lived, which allows our numerical results to agree with what we find analytically although the latter only considered cold temperatures (see Chapter 5).

Note that in Fig. 4.2 the shock wave of the sound speed for SLy EOS can be observed only in the re-scaled sub-plot. In contrast to the top right panel in Fig. 4.3 ($\rho_{0*} = 0.0032 M_{\odot}^{-2}$), we are here able to observe the shock due to a lower central rest-mass density observed by a local asymptotic observer. At low central density, such a shock was visible for all of the five EOSs considered in this thesis.

We observe in Fig. 4.3 that through the evolution of our initial data, we obtain a plateau for the lapse α, the sound speed a, the rest-mass density ρ_0 and the ADM-density ρ_{ADM}. These physical quantities represent those as measured by a "local asymptotic observer", i.e. an observer who is far from the black hole, but also well within the neutron star. We will denote these quantities with a subscript $*$. These graphs were created for a central rest-mass density of $\rho_{0*} = 0.0032 M_{\odot}^{-2} = 1.99 \times 10^{15}$ gcm^{-3} (see 6.1 for comparison).

In order to measure the accretion rate we view the rate of gas flow across the

problem which involves the evolution of a gas for which initially the fluid variables are everywhere constant on either side of an interface, but discontinuous across this interface [6].

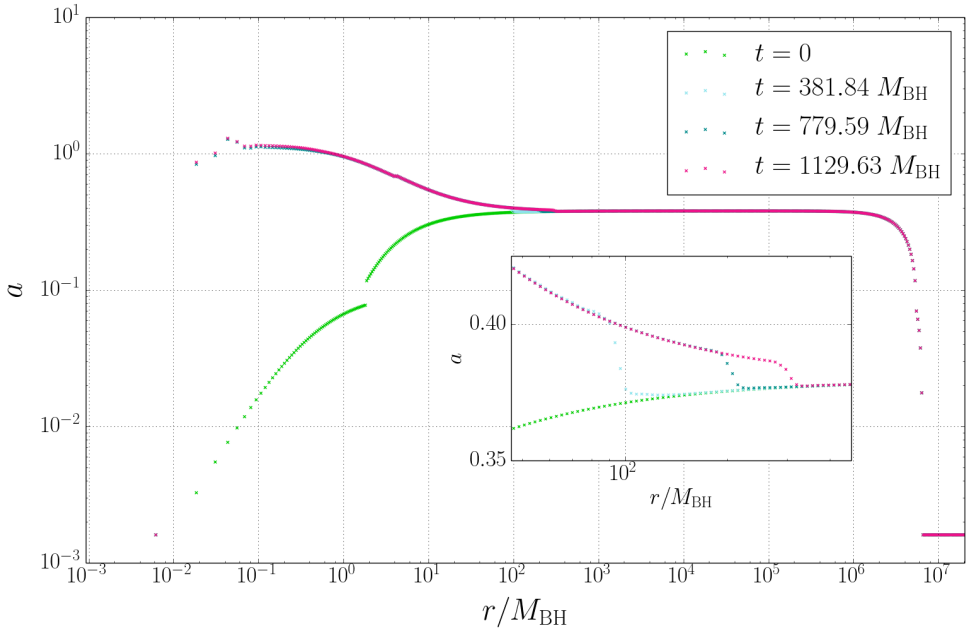

Figure 4.2: The sound speed a as a function of radius for the SLy EOS, for a neutron star with central rest-mass density $\rho_{0*} = 0.0008\ M_{\odot}^{-2}$, and a black hole with mass $M_{\rm BH} = 1.08 \times 10^{-6} M_{\odot}$ (see Table 6.1). We show profiles at four selected times including the initial time $t = 0$. During the evolution the profiles quickly settle down to an equilibrium solution. In the inset we focus on a region showing the transition from the initial data to the equilibrium solution. This transition results in a small discontinuity travelling outward that leaves, in its wake, the stationary accretion solution.

black hole's horizon. Specifically, we measure the flux $\mathcal{F}$ of rest-mass through spheres $\mathcal{S}$ with a radius r,

$$\mathcal{F}(r) = -\int_{\mathcal{S}} \sqrt{-g}\rho_0 u^r d\theta d\phi, \tag{4.3}$$

where g is the determinant of the spacetime metric (see Appendix A in [26]). The flux $\mathcal{F}$ is then evaluated on the horizon of the black hole in order to determine the accretion rate

$$\dot{M}_0 = \mathcal{F}(r_{\rm hor}). \tag{4.4}$$

We can later compare this to the analytical accretion rate obtained in Chapter

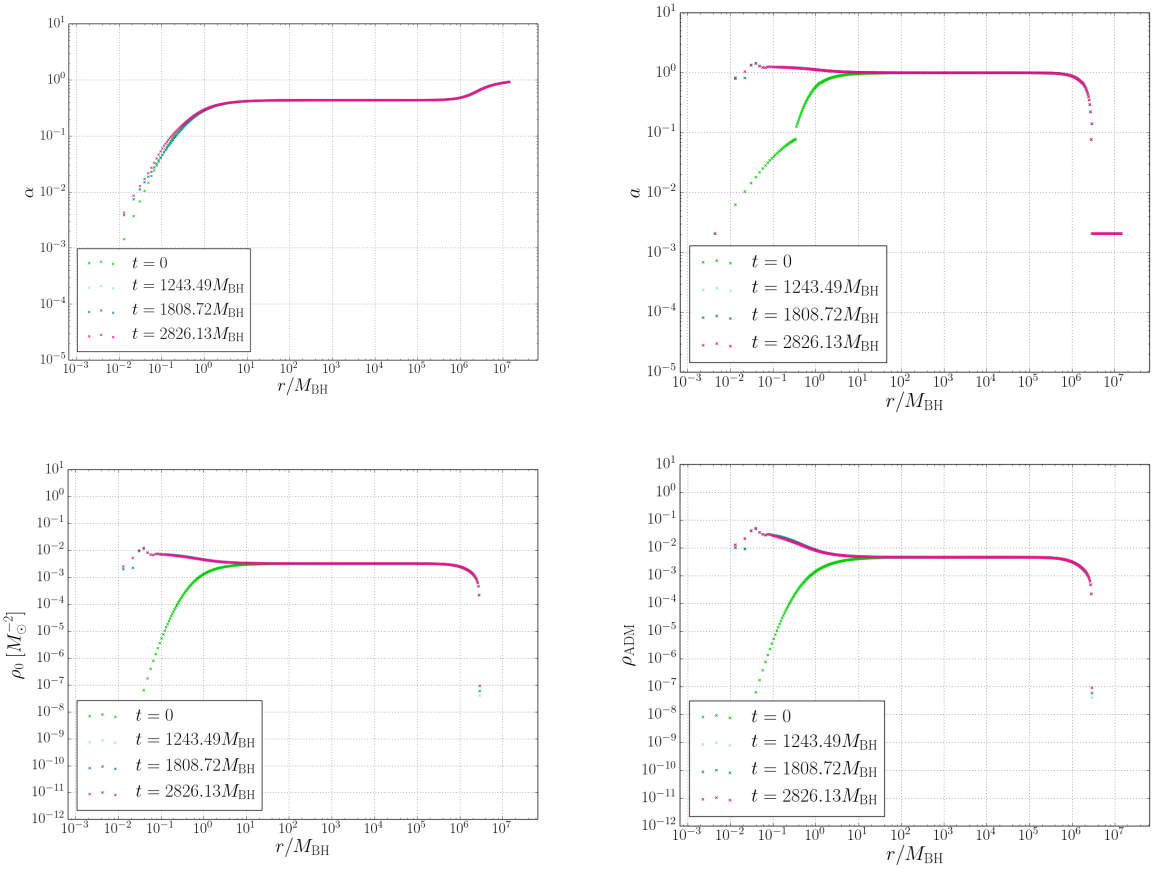

Figure 4.3: Profiles of the lapse α_* (top left), the sound speed a (top right), the rest-mass density ρ_0 (bottom left), and the ADM-density $\rho_{\rm ADM}$ (bottom right), each plotted against the radius r, for a neutron star with central rest-mass density of $\rho_0 = 0.00325 M_\odot^{-2}$ and a black hole mass $M_{\rm BH} = 1.52 \times 10^{-6} M_\odot$. The profiles are shown for four different times, including initial time $t = 0$ already shown in Fig. 4.1.

5 equation (5.22). The accretion rate in equation (4.4) quantifies the accretion of rest mass as opposed to the change of the black hole's gravitational mass. It also, contrary to (5.22), measures the accretion rate as it is seen by an observer at infinity, i.e. an observer at a large distance away from the neutron star, such that $r \gg R_{\rm NS}$. Equation (5.22) however considers a local asymptotic observer where $r \ll R_{\rm NS}$. The accretion rate measured by a "local asymptotic observer" is related to that measured at infinity by

$$\dot{M} = \alpha_* \dot{M}_0^*, \tag{4.5}$$

where α_* is the lapse function in the local asymptotic region.

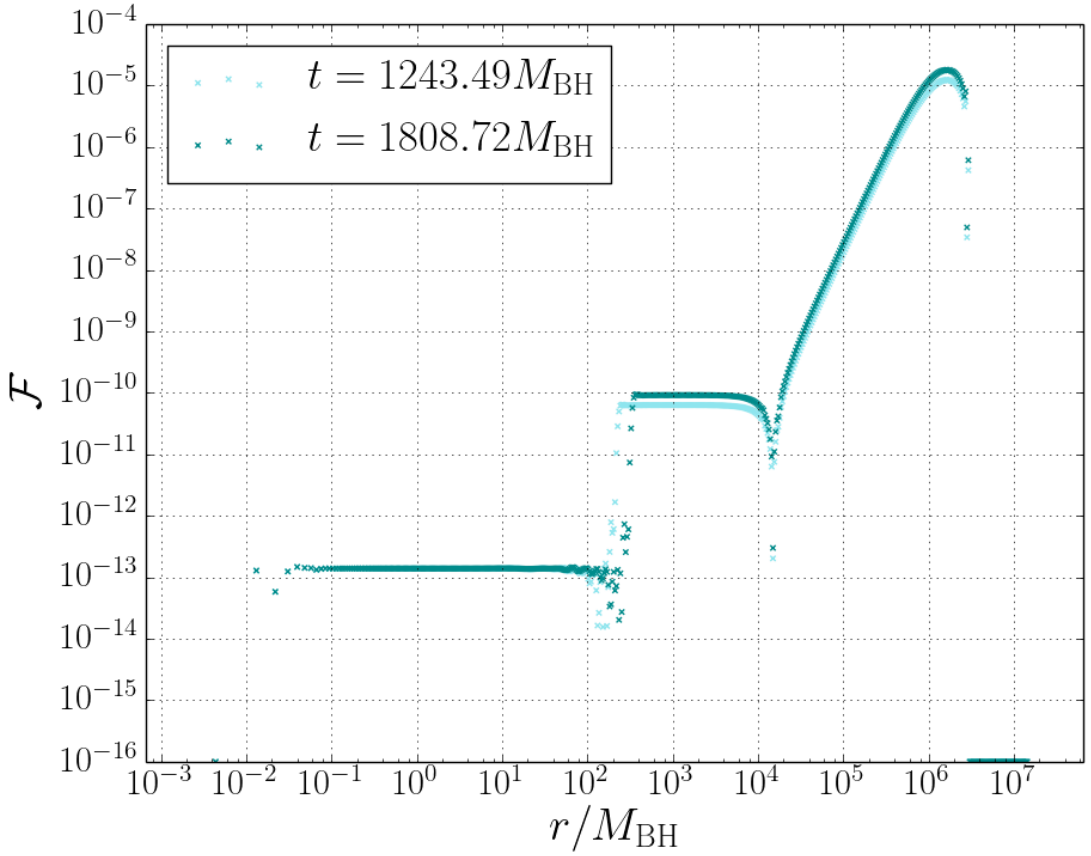

Figure 4.4: The flux $\mathcal{F}$ is plotted against the radius r for two different times with $M_{\rm BH} = 1.52 \times 10^{-6} M_\odot$ at a central rest-mass density of $\rho_0 = 0.00325 M_\odot^{-2}$. In the inner parts of the star (but outside of the black hole), we obtain the equilibrium accretion solution onto the black hole manifested by the plateau of the flux over several orders of magnitude.

In Fig. 4.4 we show the flux $\mathcal{F}$ as a function of r for different times. In particular, we observe a plateau at small radii just outside the black hole but well within the neutron star. The corresponding flux $\mathcal{F} \simeq 10^{-13}$ (in code units) is the black hole accretion rate. Note that in the outer region of the neutron star, the flux appears to be non-zero. As Richards, Baumgarte and Shapiro (2021b) note, this is due to the fact that the initial data and the numerical grid used for this simulation are not in perfect equilibrium, so that the numerical evolution leads to some adjustments.

Chapter 5

Analytical Solutions

We can use the numerical simulations in Chapter 4 to verify analytical solutions found by SBS, generalizing the results from [13, 39, 51] and RBSa. We generalize the Bondi equations [13] for general relativistic, spherical, steady-state, adiabatic accretion onto a Schwarzschild black hole of mass M, for piece wise polytropes. We use the approach described in [51] Appendix G (hereafter ST.G) until equation G.22, as there are no assumptions made about the type of EOS up until that point. After this we must employ the piece-wise approach. We will first re-create the calculations in ST.G up until G.22 in order to better comprehend the differences for the piecewise polytrope case (we will have adapted the notation in ST, to match that used in this thesis).

At infinity the gas is at rest with a baryon density n_∞, a rest-mass density $\rho_0 = m_b n_\infty$ and a total mass-energy density ρ_∞. The relation between rest-mass density and total density is given by

$$\rho = \rho_0 + (1 + \epsilon) \tag{5.1}$$

where ϵ is again our specific internal energy-density. Several conservation equations must

hold. First, baryon number must be conserved, i.e.

$$(nu^{\alpha})_{;\,\alpha} = 0, \tag{5.2}$$

as well as momentum, given by the relativistic Euler equation, as

$$(\rho + P)\, u_{\alpha;\beta}\, u^{\beta} = -P_{,\,\alpha} - u_{\alpha} P_{,\,\beta} u^{\beta} \tag{5.3}$$

where u^{α} denotes the fluid 4-velocity's components. Lastly the mass-energy density must be conserved. For this recall equation (2.7) as

$$d\left(\frac{\rho}{n}\right) + Pd\left(\frac{1}{n}\right) = Tds = 0 \tag{5.4}$$

where s is the entropy per baryon and T is the temperature. In Equation (5.4) we may rewrite the second term as

$$-Pd\left(\frac{1}{n}\right) = \frac{P}{n^2} dn \tag{5.5}$$

and the first term as

$$\left(\frac{1}{n}\frac{d\rho}{dn} - \rho\frac{1}{n^2}\right) dn = \frac{P}{n^2} dn \tag{5.6}$$

to obtain

$$\frac{d\rho}{dn} = \frac{\rho + P}{n}. \tag{5.7}$$

Additionally we can rewrite equations (5.2) and (5.3) as

$$\frac{n'}{n} + \frac{u'}{u} + \frac{2}{r} = 0, \tag{5.8}$$

and

$$uu' = -\frac{1}{\rho + P}\frac{dP}{dr}\left(1 + u^2 - \frac{2M}{r}\right) - \frac{M}{r^2} \tag{5.9}$$

in Schwarzschild coordinates.[1] In the above equations r is the areal radius and $u \equiv |u^r|$ the inward radial component of the fluid's four-velocity. The prime notation indicates differentiation with respect to r. Now we may write the sound speed as follows, using equation (5.7)

$$a^2 \equiv \left.\frac{dP}{d\rho}\right|_s = \left.\frac{dP}{dn}\right|_s \frac{n}{\rho + P}. \tag{5.10}$$

From this we can now rewrite equation (5.9) using $P' = (dP/dn)n'$ as the following:

$$uu' + \frac{M}{r^2} + a^2\frac{n'}{n}\left(1 + u^2 - \frac{2M}{r}\right) = 0. \tag{5.11}$$

Note also that we integrate (5.8) to find Equation (5.18) and integrate (5.9) to find 5.19. Next we can solve equations (5.8) and (5.11) for u' and n', yielding

$$u' = \frac{D_1}{D}, \text{ and } n' = \frac{-D_2}{D}, \tag{5.12}$$

where D_1, D_2 and D are given by

$$D_1 = \frac{1}{n}\left[\left(1 + u^2 - \frac{2M}{r}\right)\frac{2a^2}{r} - \frac{M}{r^2}\right], \tag{5.13}$$

[1]For a more information on Schwarzschild coordinates and the above see [7] and [51].

$$D_2 = \frac{2u^2/r - M/r^2}{u}, \tag{5.14}$$

and

$$D = \frac{u^2 - (1 - 2M/r + u^2)a^2}{un}, \tag{5.15}$$

respectively. In order to avoid singularities in the gas flow we must have

$$D_1 = D_2 = 0 \tag{5.16}$$

when $D = 0$. We refer to such a point as a critical point, and label all corresponding quantities with a subscript s. Then using equations (5.13-5.15) we can determine at $r = r_s$ that

$$u_s^2 = \frac{a_s^2}{1 + 3a_s^2} = \frac{M}{2r_s}. \tag{5.17}$$

Thus, we can take the integrated continuity equation (5.18), which gives the rest-mass accretion rate to be

$$4\pi\rho_0 u r^2 = \text{constant} = \dot{M}, \tag{5.18}$$

as well as the integrated Euler equation (the relativistic Bernoulli equation (ST.G.22)) to be

$$(\frac{\rho + P}{\rho_0})^2(1 - \frac{2M_{\rm BH}}{r} + u^2) = \text{constant}. \tag{5.19}$$

The above two equations are versions of equations (5.8) and (5.11), in the form of conservation equations.

Now, as opposed to continuing the calculations as done in ST and Richards,

Baumgarte and Shapiro (2021a), we implement the piecewise polytrope approach. We may write equation (5.19) as

$$\frac{\rho + P}{\rho_0} = 1 + b_i + \frac{\Gamma_i}{\Gamma_i - 1} K_i \rho_0^{\Gamma_i - 1}. \tag{5.20}$$

Now we can relate the density observed in the "local asymptotic region", denoted with the subscript $*$, with that at the critical point, using equation (2.16). We thus determine $\rho_{0s}^{\Gamma_s - 1} / \rho_{0*}^{\Gamma_* - 1}$ as follows

$$\rho_{0s}^{\Gamma_s - 1} = \frac{\Gamma_* K_*}{\Gamma_s K_s} \frac{\Gamma_* - 1 - a_*^2}{\Gamma_s - 1 - a_s^2} \frac{\Gamma_s - 1}{\Gamma_* - 1} \frac{1 + b_s}{1 + b_*} \frac{a_s^2}{a_*^2} \rho_{0*}^{\Gamma_* - 1} \tag{5.21}$$

(*cf.* eq. 10 in Richards, Baumgarte and Shapiro (2021a), hereafter Richards, Baumgarte and Shapiro (2021a).10). Now, if we insert this into equation (5.18) and use equation (5.19) we can determine the accretion rate as it is perceived by a local asymptotic observer. Here we denote these observables with the superscript $*$. We obtain

$$\dot{M}_0^* = 4\pi\lambda \left(\frac{M_{\rm BH}}{a_*^2} \right)^2 \rho_{0*} a_*, \tag{5.22}$$

where $M_{\rm BH}$ is the gravitational mass of the black hole and $\dot{M}_0^*$ is the accretion rate (the rate at which rest-mass crosses the horizon of the black hole). The above has the same form as, e.g., (ST.G.33) or (RBSa.11), except that the dimensionless accretion eigenvalue λ is instead given by

$$\lambda = \left(\frac{a_s}{a_*} \right)^{(5 - 3\Gamma_s)/(\Gamma_s - 1)} \rho_{0*}^{(\Gamma_* - \Gamma_s)/(\Gamma_s - 1)} \frac{(1 + 3a_*^2)^{3/2}}{4} \left(\frac{\Gamma_* K_*}{\Gamma_s K_s} \frac{\Gamma_* - 1 - a_*^2}{\Gamma_s - 1 - a_s^2} \frac{\Gamma_s - 1}{\Gamma_* - 1} \frac{1 + b_s}{1 + b_*} \right)^{1/(\Gamma_s - 1)}. \tag{5.23}$$

When $\Gamma_s = \Gamma_*$, $K_s = K_*$ and $b_s = b_*$, i.e. when the critical point takes on values in the same density region as the asymptotic observer, we observe that the above equation

simplifies to equation (RBSa.12).

Now we must find a relation between a_s and a_*, so that we may compute λ. We first insert equation (2.16) into (5.20) as follows

$$\frac{\rho + P}{\rho_0} = (1 + b_i)\left(1 + \frac{a^2}{\Gamma_i - 1 - a^2}\right). \tag{5.24}$$

Now we may determine the left-hand side of equation (5.19) at r_s and in the local asymptotic region, where $r_* \gg M$ and $u_* \ll 1$. Thus we obtain

$$\begin{aligned}\left(1 - \frac{2M}{r_s} + u_s^2\right)(1 + b_s)^2 \left(1 + \frac{a_s^2}{\Gamma_s - 1 - a_s^2}\right)^2 \\ = (1 + b_*)^2 \left(1 + \frac{a_*^2}{\Gamma_* - 1 - a_s^2}\right)^2\end{aligned} \tag{5.25}$$

(see ST.G.29, for comparison without piecewise polytrope). Now we may take the inverse of both sides of equation (5.25). Together with equation (5.17), we obtain

$$(1 + 3a_s^2)\left(1 - \frac{a_s^2}{\Gamma_s - 1}\right)^2 = \left(\frac{1 + b_s}{1 + b_*}\right)^2 \left(1 - \frac{a_*^2}{\Gamma_* - 1}\right)^2 \tag{5.26}$$

(*cf.* ST.G.30). Next we can rearrange this a bit to obtain

$$\frac{(3a_s^6 + (7 - 6\Gamma_s)a_s^4 + (3\Gamma_s^2 - 8\Gamma_s + 5)a_s^2)}{(\Gamma_s - 1)^2} + \left\{1 - \left(\frac{1 + b_s}{1 + b_*}\right)^2 \left(1 - \frac{a_*^2}{\Gamma_* - 1}\right)^2\right\} = 0 \tag{5.27}$$

Now, just as in the approach used in Richards, Baumgarte and Shapiro (2021a) and ST, for a single polytropic EOS, the above relation takes the form of a cubic equation where $x = a_s^2$. Thus we can write

$$x^3 + Ax^2 + Bx + C = 0 \tag{5.28}$$

with

$$
\begin{aligned}
A &= \frac{1}{3}(7 - 6\Gamma_s) \\
B &= \frac{1}{3}(1 - \Gamma_s)(5 - 3\Gamma_s) \\
C &= \frac{(\Gamma_s - 1)^2}{3}\left(1 - \left(\frac{1 + b_s}{1 + b_*}\right)^2 \left(1 - \frac{a_*^2}{\Gamma_* - 1}\right)^2\right)
\end{aligned}
\tag{5.29}
$$

where all three coefficients take on real values (see RBSa.19). However, contrary to Richards, Baumgarte and Shapiro (2021a), in this case we need to determine the constants b_i and Γ_i in the corresponding density regions ρ_{0*} and ρ_{0s}. We know how to choose b_* and Γ_* for some value of ρ_{0*}, however we do not know beforehand in which density region the critical point will be, unless the local asymptotic values are in the highest-density region, i.e. $i = 3$. In other words, to solve equation (5.26) for a_s, we must know the values of b_s and Γ_s, yet in order to determine these we must know in which region we will find a_s.

We can resolve this as follows. Let us suppose ρ_{0*} lies in the density region j. We then consider all regions $i \geq j$, assuming that, $\rho_{0s} \geq \rho_{0*}$ and solve equation (5.26), using Cardano's formula as described in Richards, Baumgarte and Shapiro (2021a). From this we then obtain candidate solutions a_{si} for each region and neglect un-physical solutions for which $a_{si}^2 < 0$. Next we evaluate equation (2.16) for remaining solutions a_{si} in the region i, retaining only candidate solutions for which the corresponding rest-mass density ρ_{0i} is actually in the region i. However, for low values of a_*, we may find feasible solutions for multiple regions, in certain cases. In these instances we must formulate the respective fluid profiles by integrating equation (5.12) both inwards and outwards away from the critical radius r_{si}.

For the EOSs considered by SBS and this thesis, at most one solution a_{si} resulted in global solutions with exactly one critical point. We adopt this solution a_{si} as the analytical Bondi profile. In Fig. 5.1 we see an example of the analytical Bondi profile for the SLy EOS in each of the four regions of density.

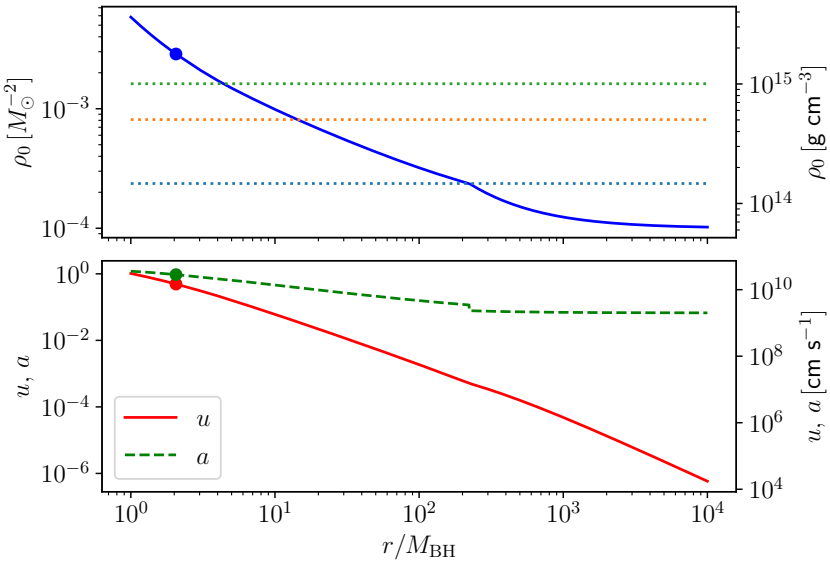

Figure 5.1: Analytical Bondi accretion profiles for the SLy EOS and an asymptotic density of $\rho_{0*} = 10^{-4} M_\odot^{-2} = 6.2 \times 10^{13}\,\mathrm{g\ cm^{-3}}$. The critical radius $r_s = 2.057\,M_{\mathrm{BH}}$ is marked by the points. The dotted horizontal lines in the top panel represent the boundary densities introduced in Fig. 2.1. We observe small discontinuities in the sound speed a at the corresponding locations [50].

Observe that the procedure explained above to find solutions a_{si} does not *necessarily* produce any solutions. In Appendix G of ST, it is shown that the existence of a critical radius is only guaranteed if all functions are continuous. In particular they claim that equation (5.15) will take on negative values for large r, but positive ones for small r, as we are approaching the black hole horizon, the D must have a zero, yielding equation (5.17). However, in our case, for the piece wise polytrope approach, D will still change signs, but it does not necessarily have to be continuous everywhere, and thus must not necessarily have a zero. All of the EOSs but MS1 yielded critical points without issues. In the case of MS1 however, we were unable to obtain any solutions, for the two small densities considered (see Table 6.1). This is related to the large discontinuity in the sound speed resulting from the large difference between Γ_2 and Γ_3 (see Chapter 6 Fig. 6.1).

Chapter 6

Results

6.1 Accretion Rates

The numerical simulations for this thesis and SBS were performed for five equations of state, as listed in Table 3.2. We determined numerical accretion rates according to equation 4.4. We determined the mass of the black hole $M_{\rm BH}$, the total gravitational mass M, the lapse as observed by a local asymptotic observer α_* and the numerical accretion rate $\dot{M}_0$ computationally as explained in Chapter 4.

In the last column of Table 6.1 the ratios of the accretion rate to the square of the black hole mass $M_{\rm BH}^2$, $\dot{M}_0/M_{\rm BH}^2$ is given and for each of the chosen equations of state. This value depends only weakly on the central density and the neutron star mass. Additionally, the value shows little variation between the different equations of state. Thus we can approximate the accretion rate for any of the given equations of state at any central density to be given by

$$\dot{M}_0 \simeq \chi (M_{\rm BH}/M_\odot)^2 \tag{6.1}$$

where $\chi \simeq 0.06$ within an approximate error of 30%. Thus the nearly universal minimum accretion rate we obtain is only slightly different from than that found in [8] (in which

EOS	ρ_{0*} [g cm^{-3}]	$M_{\rm BH}\,[M_\odot]$	$M\,[M_\odot]$	λ	$\frac{\dot M_0^*}{M_{\rm BH}^2}\,[M_\odot^{-2}]$	$\dot M_0^{*\ a}$	α_*	$\alpha_*\dot M_0^{*\ a}$	$\dot M_0{}^{\rm a}$	$\frac{\dot M_0}{M_{\rm BH}^2}\,[M_\odot^{-2}]$
SLy	1.99×10^{15}	1.52×10^{-6}	2.06	3.41	0.139	3.21×10^{-13}	0.432	1.39×10^{-13}	1.39×10^{-13}	0.060
	9.92×10^{14}	1.25×10^{-6}	1.56	1.55	0.0969	1.51×10^{-13}	0.636	9.60×10^{-14}	9.70×10^{-14}	0.062
	4.96×10^{14}	1.08×10^{-6}	0.579	0.442	0.0812	9.47×10^{-14}	0.853	8.08×10^{-14}	8.09×10^{-14}	0.069
AP3	1.68×10^{15}	1.58×10^{-6}	2.38	4.67	0.099	2.47×10^{-13}	0.398	9.83×10^{-14}	9.91×10^{-14}	0.040
	8.37×10^{14}	1.25×10^{-6}	1.61	1.68	0.0682	1.07×10^{-13}	0.645	6.90×10^{-14}	6.83×10^{-14}	0.044
	4.19×10^{14}	1.06×10^{-6}	0.402	0.254	0.0595	6.69×10^{-14}	0.890	5.95×10^{-14}	5.95×10^{-14}	0.053
AP4	1.80×10^{15}	1.55×10^{-6}	2.20	4.36	0.107	2.58×10^{-13}	0.418	1.08×10^{-13}	1.07×10^{-13}	0.045
	8.99×10^{14}	1.22×10^{-6}	1.37	1.35	0.0770	1.15×10^{-13}	0.675	7.76×10^{-14}	7.71×10^{-14}	0.052
	4.50×10^{14}	1.05×10^{-6}	0.36	0.201	0.0686	7.56×10^{-14}	0.897	6.78×10^{-14}	6.80×10^{-14}	0.062
MS1	9.30×10^{14}	1.45×10^{-6}	2.69	6.57	0.141	2.96×10^{-13}	0.474	1.40×10^{-13}	1.42×10^{-13}	0.068
	4.65×10^{14}	1.18×10^{-6}	1.54				0.717		5.38×10^{-14}	0.039
	2.33×10^{14}	1.05×10^{-6}	0.39				0.910		4.35×10^{-14}	0.039
H4	1.55×10^{15}	1.40×10^{-6}	2.00	1.98	0.176	3.45×10^{-13}	0.508	1.75×10^{-13}	1.766×10^{-13}	0.090
	7.75×10^{14}	1.24×10^{-6}	1.68	1.28	0.121	1.86×10^{-13}	0.655	1.22×10^{-13}	1.213×10^{-13}	0.079
	3.88×10^{14}	1.10×10^{-6}	0.81	0.772	0.0916	1.11×10^{-13}	0.830	9.21×10^{-14}	9.26×10^{-14}	0.077

Table 6.1: Accretion rates for different equations of state and neutron star densities, all for black holes with puncture mass $\mathcal{M} = 10^{-6}M_\odot$. The rest-mass densities ρ_{0*} refer to those observed by a local asymptotic observer, and are very similar to the central density of the corresponding neutron star in the absence of a black hole. For each EOS and central density we list, all in units of solar masses, the resulting black-hole gravitational mass $M_{\rm BH}$, the total gravitational mass M, the accretion eigenvalue λ (5.23), the value of $\dot M_0^*/M_{\rm BH}^2$ from (5.22), the resulting analytical accretion rate $\dot M_0^*$ as measured by a local asymptotic observer, this observer's value of the lapse α_* and the corresponding analytical accretion rate as measured by an observer at infinity $\alpha_*\dot M_0^*$ (see 4.5), as well as the numerical accretion rate $\dot M_0$ as computed from (4.4). For the MS1 EOS and for the smaller central densities the analytical approach of Section 5 did not yield solutions; see text for details.

[a] Values for accretion rates $\dot M_0$ in units of solar mass per year, $\dot M_0\,[M_\odot/{\rm yr}]$, can be computed from the dimensionless values $\dot M_0$ provided here using $\dot M_0\,[M_\odot/{\rm yr}] = 6.43\times10^{12}M_\odot\,{\rm yr}^{-1}\dot M_0$.

a single Γ-law was assumed). Specifically in our case with $M_\odot = 4.9 \times 10^{-6}\text{s} = 1.6 \times 10^{-13}$ yr, we can compute $\dot{M}_0$ as

$$\dot{M}_0 \simeq 4.0 \times 10^{-9} M_\odot \text{yr}^{-1} \left(\frac{M_{\text{BH}}}{10^{-10} M_\odot} \right)^{-2}. \tag{6.2}$$

This value is smaller than the $\dot{M}_0 \lesssim 3 \times 10^{-9} M_\odot \text{yr}^{-1} (M_{\text{BH}}/10^{-10} M_\odot)^{-2}$ found by [8].

Neglecting minor differences in the accretion rates (see Table 6.1), we may also integrate equation (6.1) in order to procure the neutron star's survival time

$$t_{\text{surv}} \simeq \frac{M_\odot}{\chi} \left(\frac{M_\odot}{M_0} \right) \simeq 8.2 \times 10^5 \,\text{s} \left(\frac{10^{-10} M_\odot}{M_0} \right), \tag{6.3}$$

where M_0 is the initial black hole mass, and where $\chi \simeq 0.06$ in the last equality (see [8]).

The survival time from equation (6.3) is slightly smaller, but nevertheless close to the maximum survival time determined by [7], $t_{\text{max}} \simeq 1.0 \times 10^6 \,\text{s}\,(10^{-10} M_\odot / M_0)$. This survival time has been invoked to constrain the possible masses primordial black holes might attain [18, 27] (see also [40]).

As explained in Chapter 5 (and as one can see in Table 6.1), we were unable to compute analytical accretion values for the MS1 EOS at lower densities, i.e. $\rho_{0*} = 4.56 \times 10^{14}$ and $\rho_{0*} = 2.33 \times 10^{14}$. The reason for this is the discontinuities in the sound speed for MS1 EOS, as we observe in Fig. 6.1. These discontinuities prevent the terms $M_{\text{BH}}/2r$ and $a^2/(1 + 3a^2)$ from equation (5.17) to be equal to each other, which means we are unable to find a critical point or root from the process explained in Chapter 5. This discontinuity is a peculiarity of the piecewise polytope approach, as we utilize different adiabatic indices Γ_i and constants K_i for each region of density and there are no conditions on the continuity of the sound speed.

The numerical accretion results however do exist, as the finite grid interpolates well between the discontinuities, allowing for a passing through the critical point. In other words, the numerical accretion results allow for a continuous or smooth and well-defined

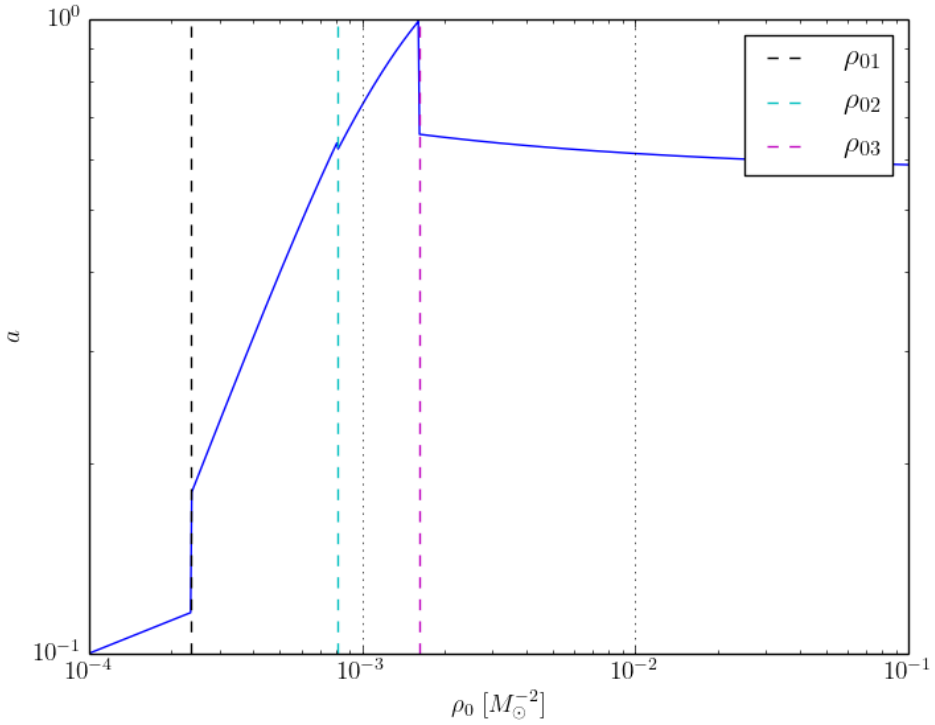

Figure 6.1: The sound speed c_s of MS1 EOS is plotted against the rest-mass density measured in $M_\odot^{-2}$. Large discontinuities or jumps can be observed at the boundary densities resulting from changes in Γ.

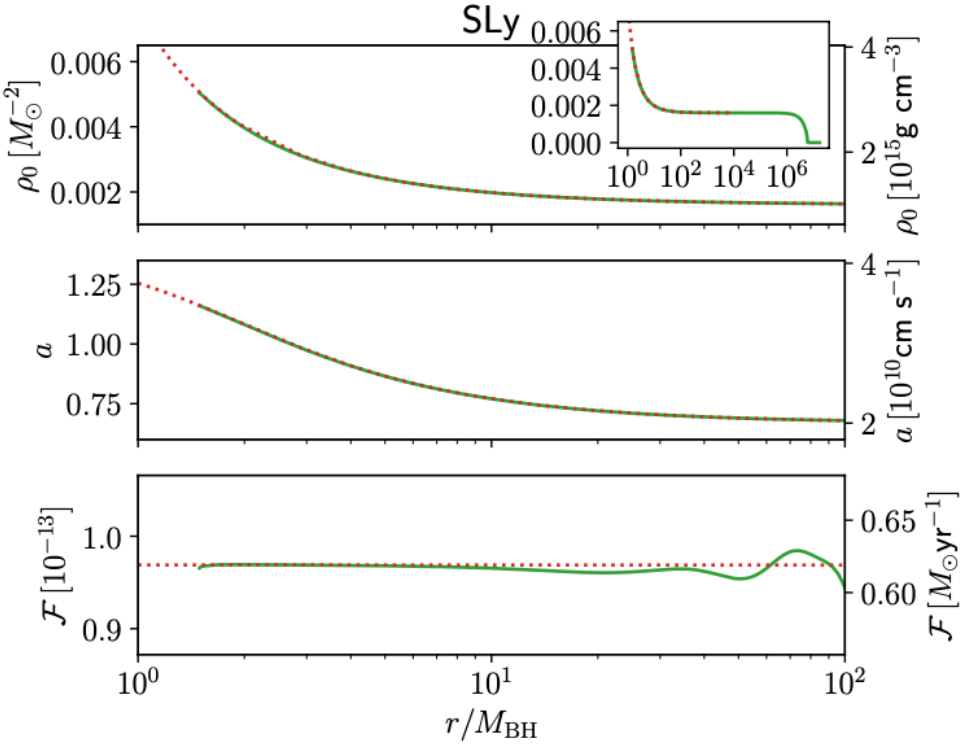

Figure 6.2: Analytical and numerical profiles of accretion flow onto the black hole embedded in the neutron star for SLy EOS, starting with a central rest-mass density of $\rho_{0*} = 0.0016 M_\odot - 2 = 9.92^{14} g\ \mathrm{cm}^{-3}$. The top panel shows the rest-mass density ρ_0, the middle one the sound speed a and the bottom one the flux $\mathcal{F}$ all plotted against the radius r. The solid, green line represents the analytical data and the dotted red line corresponds to the numerical results (see SBS Fig. 3 for more information on this figure). Note that the sound speed a exceeds the speed of light c in some regions (see also Figure 4.4

accretion flow (see Table 6.1).

We observed exceptional agreement between the analytical and numerical result for the rest-mass densities in the vicinity of the black hole, as can be seen in Fig. 6.2. The oscillations in the bottom panel of Fig. 6.2, depict the outgoing shock wave at a large distance from the black hole at the center of the star caused by the transition from the initial data to a steady state accretion solution (see SBS). Notably, we observe a shock wave for data with smaller initial densities which propagates as time passes. However, the shock causes only little heating, especially for larger initial densities and thus does not much disrupt our data. This allows us to observe good agreement of our analytical

solutions (which only consider the cold gas) with the numerical ones.

6.2 Superluminal Sound Speeds

Fig. 6.2 shows a plot of the analytically and numerically determined sound speed for SLy EOS. Both exceed the speed of light, i.e. $a > c = 1.0$ for a large part of the neutron star. Note that of the five equations of state considered in this thesis, all exhibit superluminal sound speeds at higher densities, meaning the sound speed exceeds the speed of light, i.e. $a > c$, close to the black hole. Both RBSa and East and Lehner (2019) [23] discuss the possibility of such superluminal sound speeds as a numerical artifact of the equation of state at densities higher than those found in a neutron star. East and Lehner (2019) [23] state that at densities near the accreting black hole - these densities are higher than a solitary neutron star would exhibit - nuclear equations of state may exhibit superluminal sound speeds. Thus, our observation of cases of $a > c$ are not surprising. Instead of artificially modifying these equations of state in the high-density regions in order to guarantee $a < c$ as in [23], we allow for sound speeds greater than the speed of light numerically and analytically.

Sources such as [10] have previously considered superluminal sound speeds in very dense matter. Nevertheless, while it may theoretically be possible to obtain sound speeds greater than the speed of light, there is good reason to physically reject such results based on causality. If we allowed for superluminal sound speeds we would violate a basic principle of relativity, namely that the light speed cannot be exceeded (see, e.g., [25]).

Either the piecewise polytropic representation or the equations of state themselves may be responsible for the occurrence of sound speeds greater than the speed of light. While both the EOSs and their piecewise polytope representation are constructed so that the sound speed remains subluminal for all densities up to the maximum density in static

neutron stars (i.e. stars that do not harbor black holes), our accretion results provide examples of stationary equilibrium solutions in which the $a > c$ and the densities in the ultradense region of the star significantly exceed superluminal values for systems which contain tiny black holes. Our solutions may encourage the construction of equations of state and their piecewise approximations which do not yield superluminal sound speeds at such high densities.

Chapter 7

Conclusion

In this thesis we discuss the numerical simulations and analytic calculation of accretion rates onto an endoparasitic black hole residing inside a neutron star for a family of realistic nuclear EOSs and explored the emergence of a nearly universal minimum accretion rate. The numerical results obtained agreed very well with those determined analytically in [50].

We introduce the polytropic EOSs, more realistic EOSs with nuclear matter and their piecewise approximations as described by Read et al. (2009) [45]. Unlike the strictly cold EOSs by Read et al. (2009) (goverened by only one parameter, as the temperature can be assumed negligible), we consider two parameters to describe the pressure inside the neutron star, describing warm temperatures as well. We chose representatives of four different families of EOSs namely, SLy, AP3, AP4, MS1 and H4 (see Read et al. (2009)), for the purpose of this thesis and SBS.

We outline the numerical implementation of the code used and tests of said code and discuss unit conversions of the pressure, rest-mass and total energy density as well as the constant K from the geometrized units used in the code to the more commonly understood cgs-units.

The numerical simulations and results in this thesis extend the work of East and

Lehner (2019) [23], RBSa and RBSb. We implement realistic EOSs with a piecewise polytropic representation. We perform numerical simulations, focusing on black holes wiht a mass of approximately $10^{-6}M_{\odot}$. We then support these numerical results with analytical solutions derived by SBS for stationary accretion rates onto small Schwarzschild black holes. The analytical results described are a generalization of those in Richards, Baumgarte and Shapiro (2021a) for the piecewise polytrope approach and show excellent agreement with the numerical results with some caveat.

We generalize the relativistic Bondi solutions in Richards, Baumgarte and Shapiro (2021a) and (2021b), describing accretion onto Schwarzschild black holes using realistic, nuclear EOSs approximated by piecewise polytropes. For most EOSs analytical solutions could be obtained by determining a critical point in the accretion flow, as was done in Richards, Baumgarte and Shapiro (2021a) for single Gamma-law EOSs. For some EOSs however, discontinuities in the sounds speed did not allow for analytical solutions for the accretion rate.

We find that for realistic nuclear EOSs the accretion rates depend mostly on the mass of the black hole and very little on the mass of the neutron star. The determined accretion rate is only marginally larger than the one found by [8] for single Gamma-Law EOSs. The accretion rates determined are all close to a nearly universal minimum accretion rate (see Richards, Baumgarte and Shapiro (2021a)).

However, we also observed that for certain densities the fluid profiles of several EOSs exhibited superluminal sound speeds outside the horizon of the black hole, suggesting that the EOSs are not appropriate at these densities. Any reasonable EOS and its piecewise polytropic representation should circumvent this kind of unphysical behavior at the supranuclear densities within the neutron star.

Acknowledgments

I would like to thank my honors advisor, Professor Thomas W. Baumgarte for all of the help and support. I would also like to acknowledge Professor Stuart L. Shapiro from the University of Illinois at Urbana-Champaign for his numerous contributions to this project. I would like to thank my friends and classmates for their helpful conversations and continuous support. This work was supported in part by National Science Foundation (NSF) grants No. PHY-1707526 and No. PHY-2010394 to Bowdoin College, and NSF grants No. PHY-1662211 and No. PHY-2006066 and National Aeronautics and Space Administration (NASA) grant No. 80NSSC17K0070 to the University of Illinois at Urbana-Champaign.

I would like to give special thanks to four people who have supported me throughout the process of writing this thesis. They endured my outbreaks of craziness and my tirades at LaTex as the deadline drew near and helped me reduce my stressed ice cream consumption to a more natural level. Thank you very much Sean, Teddy, Hailey and Yucheng.

References

[1] A. Akmal et al. "Equation of state of nucleon matter and neutron star structure". In: *Phys. Rev. C* 58.3 (Sept. 1998), pp. 1804–1828. arXiv: nucl-th/9804027 [nucl-th].

[2] Miguel Alcubierre et al. "Gauge conditions for long-term numerical black hole evolutions without excision". In: *Phys. Rev. D* 67.8, 084023 (2003), p. 084023. arXiv: gr-qc/0206072 [gr-qc].

[3] Thomas W. Baumgarte, Pedro J. Montero, Isabel Cordero-Carrión, et al. "Numerical relativity in spherical polar coordinates: Evolution calculations with the BSSN formulation". In: *Phys. Rev. D* 87.4, 044026 (Feb. 2013), p. 044026. arXiv: 1211.6632 [gr-qc].

[4] Thomas W. Baumgarte, Pedro J. Montero, and Ewald Müller. "Numerical relativity in spherical polar coordinates: Off-center simulations". In: *Phys. Rev. D* 91.6, 064035 (Mar. 2015), p. 064035. arXiv: 1501.05259 [gr-qc].

[5] Thomas W. Baumgarte and Stuart L. Shapiro. "Numerical integration of Einstein's field equations". In: *Phys. Rev. D* 59.2, 024007 (1999), p. 024007. arXiv: gr-qc/9810065 [gr-qc].

[6] Thomas W. Baumgarte and Stuart L. Shapiro. *Numerical Relativity: Solving Einstein's Equations on the Computer*. 2010.

[7] Thomas W. Baumgarte and Stuart Louis Shapiro. *Numerical relativity: Starting from scratch*. Cambridge University Press, 2021.

[8] Thomas W. Baumgarte and Stuart L. Shapiro. "Neutron stars harboring a primordial black hole: Maximum survival time". In: *Phys. Rev. D* 103.8, L081303 (Apr. 2021), p. L081303. arXiv: 2101.12220 [astro-ph.HE].

[9] Thomas W. Baumgarte, Stuart L. Shapiro, and Saul A. Teukolsky. "Computing Supernova Collapse to Neutron Stars and Black Holes". In: *Astrophys. J.* 443 (Apr. 1995), p. 717.

[10] S. A. Bludman and M. A. Ruderman. "Possibility of the Speed of Sound Exceeding the Speed of Light in Ultradense Matter". In: *Physical Review* 170.5 (June 1968), pp. 1176–1184.

[11] C. Bona et al. "New Formalism for Numerical Relativity". In: *Phys. Rev. Lett.* 75 (1995), pp. 600–603.

[12] Silvano Bonazzola et al. "Constrained scheme for the Einstein equations based on the Dirac gauge and spherical coordinates". In: *Phys. Rev. D* 70.10, 104007 (2004), p. 104007. arXiv: gr-qc/0307082 [gr-qc].

[13] H. Bondi. "On spherically symmetrical accretion". In: *Mon. Not. R. Astron. Soc.* 112 (Jan. 1952), p. 195.

[14] Joseph Bramante and Fatemeh Elahi. "Higgs portals to pulsar collapse". In: *Phys. Rev. D* 91.11, 115001 (June 2015), p. 115001. arXiv: 1504.04019 [hep-ph].

[15] Joseph Bramante and Tim Linden. "Detecting Dark Matter with Imploding Pulsars in the Galactic Center". In: *Phys. Rev. Lett.* 113.19, 191301 (Nov. 2014), p. 191301. arXiv: 1405.1031 [astro-ph.HE].

[16] Joseph Bramante, Tim Linden, and Yu-Dai Tsai. "Searching for dark matter with neutron star mergers and quiet kilonovae". In: *Phys. Rev. D* 97.5, 055016 (Mar. 2018), p. 055016. arXiv: 1706.00001 [hep-ph].

[17] J. David Brown. "Covariant formulations of Baumgarte, Shapiro, Shibata, and Nakamura and the standard gauge". In: *Phys. Rev. D* 79.10, 104029 (2009), p. 104029. arXiv: 0902.3652 [gr-qc].

[18] Fabio Capela et al. "Constraints on primordial black holes as dark matter candidates from capture by neutron stars". In: *Phys. Rev. D* 87.12, 123524 (June 2013), p. 123524. arXiv: 1301.4984 [astro-ph.CO].

[19] Bernard Carr and Florian Kühnel. "Primordial Black Holes as Dark Matter: Recent Developments". In: *Annual Review of Nuclear and Particle Science* 70 (Oct. 2020), pp. 355–394. arXiv: 2006.02838 [astro-ph.CO].

[20] Bernard Carr, Kazunori Kohri, et al. "Constraints on Primordial Black Holes". In: *arXiv e-prints*, arXiv:2002.12778 (Feb. 2020), arXiv:2002.12778. arXiv: 2002.12778 [astro-ph.CO].

[21] F. Douchin and P. Haensel. "A unified equation of state of dense matter and neutron star structure". In: *Astronomy and Astrophysics* 380 (Dec. 2001), pp. 151–167. arXiv: astro-ph/0111092 [astro-ph].

[22] Leanne D. Duffy and Karl van Bibber. "Axions as dark matter particles". In: *New Journal of Physics* 11.10, 105008 (Oct. 2009), p. 105008. arXiv: 0904.3346 [hep-ph].

[23] William E. East and Luis Lehner. "Fate of a neutron star with an endoparasitic black hole and implications for dark matter". In: *Phys. Rev. D* 100.12, 124026 (2019), p. 124026. arXiv: 1909.07968 [gr-qc].

[24] B. Einfeldt. "On Godunov methods for gas dynamics". In: *SIAM J. Numer. Anal.* 25 (1988), p. 294.

[25] George F. R. Ellis et al. "Causality and the speed of sound". In: *General Relativity and Gravitation* 39.10 (2007), pp. 1651–1660. arXiv: gr-qc/0703121 [gr-qc].

[26] Brian D. Farris et al. "Binary black hole mergers in gaseous environments: "Binary Bondi" and "binary Bondi-Hoyle-Lyttleton" accretion". In: *Phys. Rev. D* 81.8, 084008 (2010), p. 084008. arXiv: 0912.2096 [astro-ph.HE].

[27] Y. Génolini et al. “Revisiting primordial black hole capture into neutron stars”. In: *Phys. Rev. D* 102.8, 083004 (Oct. 2020), p. 083004. arXiv: 2006.16975 [astro-ph.HE].

[28] Itzhak Goldman and Shmuel Nussinov. “Weakly interacting massive particles and neutron stars”. In: *Phys. Rev. D* 40.10 (Nov. 1989), pp. 3221–3230.

[29] Eric Gourgoulhon. *3+1 Formalism in General Relativity*. Springer, Berlin, 2012.

[30] A. Harten et al. “On upstream differencing and Godunov type methods for hyperbolic conservation laws”. In: *SIAM Rev.* 25 (1983), pp. 35–61.

[31] Stephen Hawking. “Gravitationally collapsed objects of very low mass”. In: *Mon. Not. R. Astron. Soc.* 152 (Jan. 1971), p. 75.

[32] Chris Kouvaris and Peter Tinyakov. “Growth of black holes in the interior of rotating neutron stars”. In: *Phys. Rev. D* 90.4, 043512 (Aug. 2014), p. 043512. arXiv: 1312.3764 [astro-ph.SR].

[33] Florian Kühnel and Katherine Freese. “Constraints on primordial black holes with extended mass functions”. In: *Phys. Rev. D* 95.8, 083508 (Apr. 2017), p. 083508. arXiv: 1701.07223 [astro-ph.CO].

[34] Benjamin D. Lackey. “The neutron-star equation of state and gravitational waves from compact binaries”. PhD thesis. The University of Wisconsin - Milwaukee, Jan. 2012.

[35] Benjamin D. Lackey et al. “Observational constraints on hyperons in neutron stars”. In: *Phys. Rev. D* 73.2, 024021 (Jan. 2006), p. 024021. arXiv: astro-ph/0507312 [astro-ph].

[36] James M. Lattimer. “The Nuclear Equation of State and Neutron Star Masses”. In: *Annual Review of Nuclear and Particle Science* 62.1 (Nov. 2012), pp. 485–515. arXiv: 1305.3510 [nucl-th].

[37] Arnaud de Lavallaz and Malcolm Fairbairn. “Neutron stars as dark matter probes”. In: *Phys. Rev. D* 81.12, 123521 (June 2010), p. 123521. arXiv: 1004.0629 [astro-ph.GA].

[38] D. Markovic. “Evolution of a primordial black hole inside a rotating solar-type star”. In: *Mon. Not. R. Astron. Soc.* 277.1 (Nov. 1995), pp. 25–35.

[39] F. Curtis Michel. “Accretion of Matter by Condensed Objects”. In: *Astrophys. Space Sci.* 15.1 (Jan. 1972), pp. 153–160.

[40] Paulo Montero-Camacho et al. “Revisiting constraints on asteroid-mass primordial black holes as dark matter candidates”. In: *Journal of Cosmology and Astroparticle Physics* 2019.8, 031 (Aug. 2019), p. 031. arXiv: 1906.05950 [astro-ph.CO].

[41] I. A. Morrison et al. “The Moment of Inertia of the Binary Pulsar J0737-3039A: Constraining the Nuclear Equation of State”. In: *Astrophys. J. Lett.* 617.2 (Dec. 2004), pp. L135–L138. arXiv: astro-ph/0411353 [astro-ph].

[42] Horst Müller and Brian D. Serot. “Relativistic mean-field theory and the high-density nuclear equation of state”. In: *Nucl. Phys. A* 606 (1996), pp. 508–537. arXiv: nucl-th/9603037 [nucl-th].

[43] T. Nakamura et al. “General Relativistic Collapse to Black Holes and Gravitational Waves from Black Holes”. In: *Progress of Theoretical Physics Supplement* 90 (1987), pp. 1–218.

[44] J. R. Oppenheimer and G. M. Volkoff. “On Massive Neutron Cores”. In: *Physical Review* 55.4 (Feb. 1939), pp. 374–381.

[45] Jocelyn S. Read et al. “Constraints on a phenomenologically parametrized neutron-star equation of state”. In: *Phys. Rev. D* 79.12, 124032 (2009), p. 124032. arXiv: 0812.2163 [astro-ph].

[46] Chloe B. Richards. “Accretion onto endoparasitic black holes at the center of neutron stars”. 2021.

[47] Chloe B. Richards, Thomas W. Baumgarte, et al. “Relativistic Bondi accretion for stiff equations of state”. In: *Mon. Not. R. Astron. Soc.* 502.2 (Apr. 2021), pp. 3003–3011. arXiv: 2101.08797 [astro-ph.HE].

[48] Chloe B. Richards, Thomas W. Baumgarte, et al. “Accretion onto a small black hole at the center of a neutron star”. In: *Phys. Rev. D* 103.10, 104009 (May 2021), p. 104009. arXiv: 2102.09574 [astro-ph.HE].

[49] Misao Sasaki et al. “Primordial black holes—perspectives in gravitational wave astronomy”. In: *Classical and Quantum Gravity* 35.6, 063001 (Mar. 2018), p. 063001. arXiv: 1801.05235 [astro-ph.CO].

[50] Sophia C. Schnauck et al. “Accretion onto black holes inside neutron stars with realistic nuclear equations of state: analytic and numerical treatments”. In: *arXiv e-prints* (Oct. 2021). arXiv: 2110.08285 [astro-ph.HE].

[51] Stuart L. Shapiro and Saul A. Teukolsky. *Black Holes, White Dwarfs and Neutron Stars: The Physics of Compact Objects*. 1986.

[52] Masaru Shibata and Takashi Nakamura. “Evolution of three-dimensional gravitational waves: Harmonic slicing case”. In: *Phys. Rev. D* 52.10 (1995), pp. 5428–5444.

[53] Masaru Shibata, Kōji Uryū, et al. “Deriving formulations for numerical computation of binary neutron stars in quasicircular orbits”. In: *Phys. Rev. D* 70.4, 044044 (2004), p. 044044. arXiv: gr-qc/0407036 [gr-qc].

[54] Marcus Thierfelder et al. “Numerical relativity simulations of binary neutron stars”. In: *Phys. Rev. D* 84.4, 044012 (2011), p. 044012. arXiv: 1104.4751 [gr-qc].

[55] Richard C. Tolman. “Static Solutions of Einstein’s Field Equations for Spheres of Fluid”. In: *Physical Review* 55.4 (Feb. 1939), pp. 364–373.

[56] B. van Leer. “Towards the ultimate conservative difference scheme: IV. A new approach to numerical convection”. In: *Journal of Computational Physics* 23 (1977), pp. 276–299.

[57] Ville Vaskonen and Hardi Veermäe. “Did NANOGrav See a Signal from Primordial Black Hole Formation?” In: *Phys. Rev. Lett.* 126.5, 051303 (Feb. 2021), p. 051303. arXiv: 2009.07832 [astro-ph.CO].